

## THE MEGASECOND *CHANDRA* XVP OBSERVATION OF NGC 3115: WITNESSING THE FLOW OF HOT GAS WITHIN THE BONDI RADIUS

KA-WAH WONG<sup>1</sup>, JIMMY A. IRWIN<sup>1</sup>, ROMAN V. SHCHERBAKOV<sup>2,3</sup>, MIHOKO YUKITA<sup>1,4</sup>, EVAN T. MILLION<sup>1</sup>, AND JOEL N. BREGMAN<sup>5</sup>

*Astrophysical Journal, submitted*

### ABSTRACT

Observational confirmation of hot accretion model predictions has been hindered by the challenge to resolve spatially the Bondi radii of black holes with X-ray telescopes. Here, we use the Megasecond *Chandra* X-ray Visionary Project (XVP) observation of the NGC 3115 supermassive black hole to place the first direct observational constraints on the spatially and spectroscopically resolved structures of the X-ray emitting gas inside the Bondi radius of a black hole. We measured temperature and density profiles of the hot gas from a fraction out to tens of the Bondi radius ( $R_B = 2''.4\text{--}4''.8 = 112\text{--}224$  pc). The projected temperature jumps significantly from  $\sim 0.3$  keV beyond  $5''$  to  $\sim 0.7$  keV within  $\sim 4''\text{--}5''$ , but then abruptly drops back to  $\sim 0.3$  keV within  $\sim 3''$ . This is contrary to the expectation that the temperature should rise toward the center for a radiatively inefficient accretion flow. A hotter thermal component of  $\sim 1$  keV inside  $3''$  ( $\sim 150$  pc) is revealed using a two component thermal model, with the cooler  $\sim 0.3$  keV thermal component dominating the spectra. We argue that the softer emission comes from diffuse gas physically located within  $\sim 150$  pc from the black hole. The density profile is broadly consistent with  $\rho \propto r^{-1}$  within the Bondi radius for either the single temperature or the two-temperature model. The X-ray data alone with physical reasoning argue against the absence of a black hole, supporting that we are witnessing the onset of the gravitational influence of the supermassive black hole.

*Subject headings:* accretion, accretion disks — black hole physics — galaxies: elliptical and lenticular, cD — galaxies: individual (NGC 3115) — galaxies: nuclei — X-rays: galaxies

### 1. INTRODUCTION

Understanding how supermassive black holes accrete matter from their galactic surroundings is an important, yet still poorly understood process. While spectacular in nature, quasars accreting at  $\sim 10\%$  of their Eddington limit with luminosities of  $\sim 10^{46}$  ergs  $s^{-1}$  do not represent the current behavior of the vast majority of supermassive black holes. Even more mildly accreting ( $\sim 10^{-5}L_{\text{Edd}}$ ) black holes classified as AGN only constitute a few percent or less of the supermassive black hole population depending on environment (e.g., Dressler & Gunn 1983; Huchra & Burg 1992; Ho 2008, 2009). Instead, nearly all supermassive black holes exhibit a much more modest ( $< 10^{-8}L_{\text{Edd}}$ ) radiatively inefficient accretion mode, notably illustrated by the quiescent 4 million solar mass black hole at the center of the Milky Way.

The well known classical Bondi accretion model (Bondi 1952) suggests that in order to be accreted, gas must be within a distance from the black hole where the gravitational potential of the black hole dominates the thermal energy of the hot gas. The “sphere of influence” for gas around a black hole is defined by its Bondi radius,  $R_B = 2GM_{\text{BH}}/c_s^2$ , where  $M_{\text{BH}}$  is the mass of the black

hole, and  $c_s$  is the sound speed of gas far away from the black hole. For a billion solar mass black hole with hot gas temperature of  $\sim 0.1\text{--}1$  keV, the Bondi radius is on the order of tens to hundreds of parsecs, or 5–6 orders of magnitude greater than the Schwarzschild radius of the black hole ( $R_S = 2GM_{\text{BH}}/c^2$ ). Although realistic astrophysical accretion may be dramatically different from the Bondi accretion model due to its simple idealized assumptions, studying hot gas properties within the Bondi “sphere of influence” remains crucial for understanding how matter is being accreted.

It is not the case that very low-luminosity black holes are simply starved for gas. For example, the Bondi rate of gas flowing through the Bondi radius of Sgr A\* at the center of the Milky Way ( $\dot{M}_B \sim 10^{-6} M_\odot \text{ yr}^{-1}$ ; Baganoff et al. 2003) would imply a luminosity of  $\sim 10^{41}$  ergs  $s^{-1}$  at the standard 10% radiative efficiency (e.g., Fabian & Rees 1995), several orders of magnitude higher than is observed (Narayan et al. 1998, and references therein). Two general solutions have been proposed to account for the missing radiative energy. One solution is that although matter passing through the Bondi radius makes it to the event horizon of the black hole, most of the energy in the gas is carried by the ions, and is advected down the black hole before radiating much energy (advection-dominated accretion flows, or ADAFs; Ichimaru 1977; Rees et al. 1982; Narayan & Yi 1994). The second solution is that matter passing through the Bondi region does not make it to the event horizon of the black hole, but either circulates in convective eddies (convective-dominated accretion flows, or CDAFs; Narayan et al. 2000; Quataert & Gruzinov

kw6k@email.virginia.edu

<sup>1</sup> Department of Physics and Astronomy, University of Alabama, Box 870324, Tuscaloosa, AL 35487, USA

<sup>2</sup> Department of Astronomy, University of Maryland, College Park, MD 20742-2421, USA

<sup>3</sup> Hubble Fellow

<sup>4</sup> Johns Hopkins University, Homewood Campus, Baltimore, MD, 21218, USA

<sup>5</sup> Department of Astronomy, University of Michigan, 500 Church Street, Ann Arbor, MI 48109-1042, USA

2000; Abramowicz et al. 2002), or some of the gas actually escapes the potential of the black hole in an outflow (such as advection-dominated inflow-outflow solutions, or ADIOS; Blandford & Begelman 1999; Begelman 2012), or variations on these themes.

Ideally, one would like to compare the predictions of radiatively inefficient accretion flow models with the X-ray-determined properties of the hot gas flowing from the galactic potential into the Bondi region (Brighenti & Mathews 1999; Quataert & Narayan 2000). Most notably the temperature and density profiles of the hot gas provide leverage for distinguishing among competing accretion flow models. However, observational confirmation of predictions of these theories has been hindered by the inability to resolve spatially the Bondi radii of black holes with X-ray telescopes. For even the closest, most massive black holes, the angular size of the Bondi regions are on the order of only a few arcseconds or less (Garcia et al. 2010). Sgr A\* is by far the best-studied Bondi region both observationally and theoretically (e.g., Yuan et al. 2002, 2003; Baganoff et al. 2003; Shcherbakov & Baganoff 2010; Wang et al. 2013), but with a detected size of only  $1''.5$  in X-ray, simultaneous spatial and spectral analysis is challenging. Few Bondi regions with radii exceeding  $2''$  are accessible with *Chandra*, and these candidates suffer from the presence of a bright point source in or near the nucleus of the galaxy (M87) or low X-ray gas count rates (NGC 3115), or both (M31\*).

Despite its low X-ray count rate, the gas surrounding the black hole in NGC 3115 provides us with the best opportunity to obtain spatially-resolved spectral information on the hot gas within the Bondi region of a black hole. At a distance of 9.7 Mpc (Tonry et al. 2001), NGC 3115 is the nearest galaxy with a one to two billion solar mass black hole (Kormendy et al. 1996; Emsellem et al. 1999). The low temperature ( $\sim 0.3$  keV) of the ambient gas implies a Bondi radius of  $R_B = 112\text{--}224$  pc =  $2''.4\text{--}4''.8$  (Wong et al. 2011, hereafter W11). Previous moderate length *Chandra* observations of NGC 3115 revealed evidence for an increase in the hot gas temperature inside the Bondi region of its supermassive black hole (W11), one of the tell-tale signatures of most (non-cooling) accretion flow models. W11 also found the slope of the density of the hot gas inside the Bondi radius to be  $\rho \sim r^{-1}$ , although neither the temperature spike nor the density slope could be constrained to high significance owing to the low X-ray count rate. The tantalizing results prompted a deeper 1 Megasecond *Chandra* X-ray Visionary Project (XVP) observation of NGC 3115 to collect the required number of X-ray photons to derive temperature and density profiles on a spatial scale that matches the resolution of *Chandra*.

Here we describe the results from our analysis of the *Chandra* Megasecond observation of NGC 3115. After careful subtraction of contaminating X-ray emission from other sources, we derive the first spatially-resolved temperature and density profiles of gas inside the Bondi region of a black hole. In a companion paper (Shcherbakov et al. 2013), we develop radial gas flow models for NGC 3115.

The paper is organized as follows. Section 2 describes the X-ray observations and data analysis. In Section 3,

we examine the spatially extended nature of the hot gas within the Bondi radius and address the lack of evidence of X-ray emission from the central weak AGN. Section 4 describes the observational results, in particular, the temperature, surface brightness, and density profiles of the hot gas, as well as an unexpected strong soft emission within the Bondi radius, and evidence of a (at least) two-temperature structure of the hot gas within  $\sim 150$  pc from the black hole. We discuss possible origins of the central soft emission in Section 5. We argue against the idea that spun-up stars can be an important X-ray component at the NGC 3115 center in Section 6. The implications to accretion models are discussed in Section 7. We summarize and conclude in Section 8. Systematic uncertainties in spectral modeling is addressed in detail in Appendix A. The X-ray upper limit of the central weak AGN is assessed in Appendix B.

At a distance of 9.7 Mpc, the angular scale of NGC 3115 is  $47$  pc/ $1''$ . Unlike our previous paper (W11) which presents  $1\sigma$  confidence, errors are given at 90% confidence level in this paper unless otherwise specified.

## 2. X-RAY OBSERVATIONS AND SPECTRAL ANALYSIS

### 2.1. Data Reduction

NGC 3115 (Figure 1) was observed eight times with the *Chandra* in 2012 between January and April (ObsIDs 13817, 13819, 13820, 13821, 13822, 14383, 14384, and 14419) for a total of 998 ks. Unless otherwise specified, we only included all these 2012 observations in the data analysis but do not include the 155 ks observations taken in 2001 (ObsID 2040) and 2010 (ObsIDs 11268 and 12095) because the effective area has changed dramatically even since 2010 due to the increasing Advanced CCD Imaging Spectrometer (ACIS) contamination. We note that including the 2001 and 2010 observations generally introduced a  $\lesssim 10\text{--}20\%$  systematic error in the spectral analysis but does not improve the statistical uncertainties. In all the observations NGC 3115 was placed near the ACIS-S aimpoint. All the data were reprocessed using the `chandra_repro` script of CIAO 4.4 and CALDB 4.4.10. The default sub-pixel event-repositioning algorithm “EDSER” was used. After removed flares using the CIAO `deflare` script, the cleaned exposure time was 972 ks.

To improve the astrometry between different observations required for the high spatial resolution analysis, we have performed relative astrometry correction for each observation. We first created a sub-pixel resolution image in 0.3–6.0 keV with a binning size of  $0.123''$  (0.25 ccd pixel) for a  $\sim 4 \times 4$  square arcmin region around NGC 3115 for each observation. We then used the CIAO `wavdetect` script to create an initial source list for each image. This source list was only used for astrometry correction. The longest observation (ObsID 13820) was used as the reference for the relative astrometry corrections. The CIAO `reproject_aspect` script was then used to create new aspect solutions for all the other observations. All of the data were reprocessed again using `chandra_repro` with the new aspect solutions to complete the astrometry corrections.

We extracted a local background from a  $70''\text{--}90''$  annular region far enough from the center of NGC 3115 so that the source-removed surface brightness of the X-ray

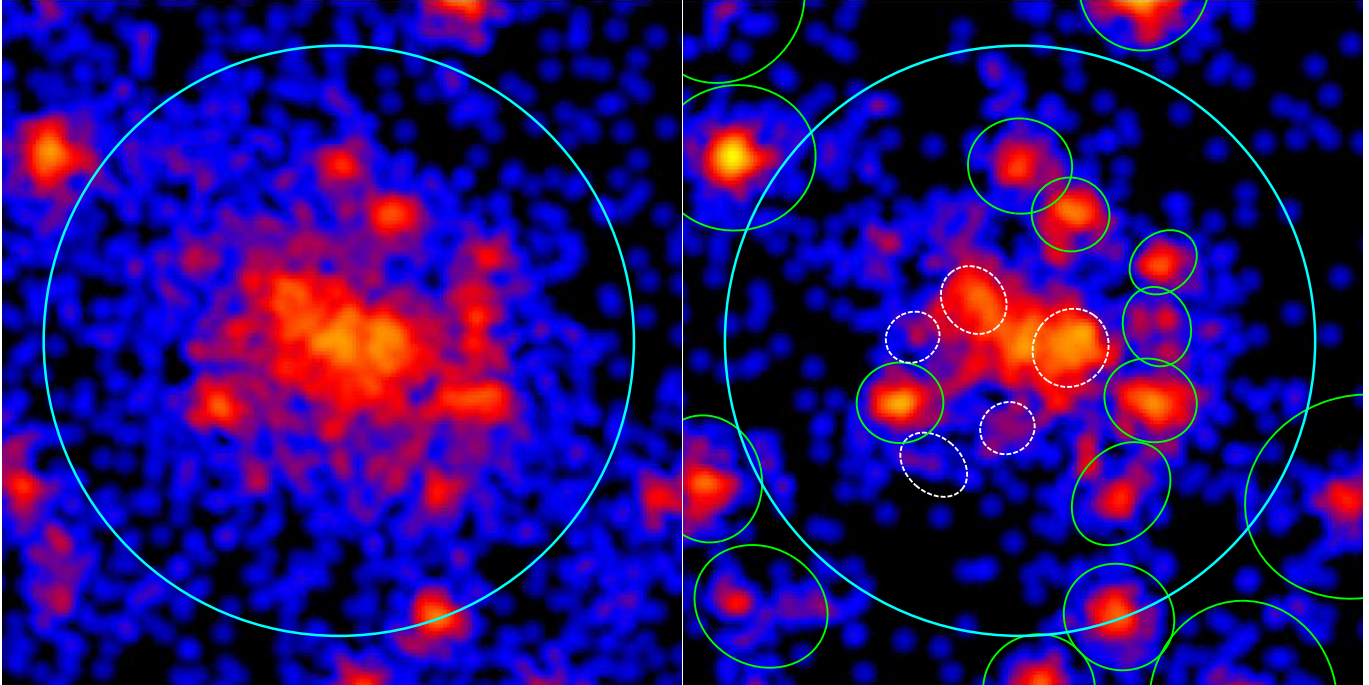


FIG. 1.— Smoothed soft band (0.5–1.0 keV: left) and hard band (2.0–6.0 keV: right) *Chandra* sub-pixel resolution images of NGC 3115 with 1 image pixel binning size =  $0''.0615$ . Both images were smoothed with a Gaussian kernel of FWHM =  $0''.3$ . North is top while east is left. The large circles (cyan) are centered on the extended emission; each has a radius of  $5'' (=235 \text{ pc})$ . The point sources (or compact structures) removed are shown in smaller solid green and dashed white ellipses, with the dashed white ellipse sources only detected on sub-pixel resolution images (see text). The unresolved diffuse emission in the soft band image is dominated by hot gas beyond  $\gtrsim 2''$  while the hard band image is dominated by LMXBs. Note the more extended and rounder extended emission in the soft band compared to the narrower extended structure of the hard emission inside  $2''\text{--}3''$ , with the orientation of the hard emission roughly aligned with the major axis of the optical emission along the NE-SW direction (Kormendy et al. 1996).

emission is basically flat. Background contributes negligibly to the inner  $\sim 10''$  but becomes significant only in the outermost regions (Appendix A). Changing the background level by  $\pm 10\%$  introduces systematic uncertainties that are much smaller than the statistical uncertainties within  $20''$ . It only introduces a systematic uncertainty that is larger than the statistical uncertainty in gas temperature beyond  $20''$ , although the gas normalization is still hardly affected.

### 2.2. Point Source Removal

To analyze the diffuse X-ray emission of the hot gas it is necessary to remove contaminating point sources (or compact structures). Point sources were detected with CIAO `wavdetect`. To detect as many point sources as possible, we used all the observations except the data taken in 2001 because its optical axis position is significantly different ( $> 1'$ ) from the other observations. We created images with 1 ccd pixel binning size in four energy bands (0.3–1.0, 1.0–2.0, 2.0–6.0, and 0.3–6.0 keV) and combined images according to energy bands in these observations. The source regions in different energy bands were then visually inspected and combined. We refined the region sizes of the point sources (or compact structures) detected within  $4''$  by using sub-pixel images with 0.125 pixel binning size and ran CIAO `wavdetect` again. With these sub-pixel images, a few more weak sources and also some elongated structures were identified within  $3''$  (Figure 1). Unless otherwise specified, we have removed all these structures except for the source detected at the galaxy center in our nominal data analysis. Including or removing these structures within  $3''$

gives essentially the same results for the gas component.

As mentioned above, the central peak was detected with `wavdetect`. Our analysis shows no strong evidence of a point source and the central peak is clearly extended (Section 3). We have determined the upper limit of the potential point source and found that hot gas measurements are not affected by this potential weak AGN (Section 3 and Appendix B). Therefore, we did not remove the central region and we ignored any potential AGN contamination in our analysis.

### 2.3. Spectral Analysis

We extracted spectra in circular annuli centered on the central peak of the extended X-ray emission (0.3–6.0 keV), which is assumed to be the center of the flow (the supermassive black hole). This peak is within  $\lesssim 0''.05$  of the soft (0.3–2.0 keV) emission peak. It is separated by  $0''.15$  from the optical peak we measured using the archival *HST* data (below), consistent with the position uncertainty. The diffuse gas distribution is assumed to be spherically symmetric which is justified in Section 4.2. All the spectra were analyzed using the X-ray Spectral Fitting Package<sup>6</sup> (`XSPEC`).

The unresolved X-ray emission is mainly contributed by unresolved low-mass X-ray binaries (LMXBs), stellar emission from cataclysmic variables and coronally active binaries (CV/ABs), and the diffuse hot gas component that we are interested in. After the CV/AB component is spectrally-subtracted in a statistical manner (described below), the very soft emission from the gas and the very

<sup>6</sup> <http://heasarc.nasa.gov/xanadu/xspec/>

hard emission from the unresolved LMXBs can be reliably separated through spectral fitting. The combined spectra of resolved low- $L_X$  ( $< 10^{37}$  ergs s $^{-1}$ ) LMXBs in the bulge of M31 are very similar to more luminous LMXBs (Irwin et al. 2003). Therefore, we can assume the unresolved LMXB emission to be spectrally modeled as the brighter resolved sources. With our deep Megasecond observation, many more LMXBs were detected than in W11, and the unresolved LMXBs are no longer the dominant component at  $\gtrsim 2''$  in the 0.5–1.0 keV band (Figure 5 below). We modeled the LMXB component as a power law model and fixed the power-index to  $\Gamma_{\text{LMXB}} = 1.6$  which is consistent with the value of  $1.61_{-0.02}^{+0.02}$  measured from the combined spectrum of all the resolved point sources within  $D_{25}$  of NGC 3115 and the value (1.6) of the summed emission from many resolved X-ray binaries in nearby galaxies (Irwin et al. 2003). Using  $\Gamma_{\text{LMXB}} = 1.4$  or 1.8 gives essentially the same results for the analysis of the hot gas (Appendix A).

The faint and soft sources similar to those of the Galactic Ridge emission (CV/AB) contribute appreciably to the X-ray flux beyond the Bondi region. Hence, including this component is essential in the analysis. In W11, we used the 2MASS K-band image to estimate the CV/AB contribution, and assumed the X-ray flux of the CV/AB component scales linearly with the K-band luminosity. Because the typical spatial resolution of 2MASS is about  $2''$ – $3''$  which is poorer than the *Chandra* resolution, the CV/AB in the central regions can be underestimated.

In this paper, we use a higher resolution *HST* WFPC2 I-band (F814W filter) image to estimate the CV/AB contribution. We assume the intrinsic K-band surface brightness profile follows the I-band surface brightness profile. The archival *HST* I-band image has a PSF FWHM and a pixel size of  $\sim 0''.1$  which is much smaller than the 2MASS PSF ( $2''$ – $3''$ ) and is close to the *Chandra* PSF ( $\sim 0''.5$  near the aimpoint). Therefore, we can use the *HST* I-band surface brightness profile to estimate the intrinsic K-band surface brightness profile. In practice, we first smoothed the *HST* I-band image with a Gaussian kernel. We then re-scaled the *HST* I-band image to match the 2MASS flux unit within a radius of  $10''$  centered at the surface brightness peak. After that, we generated a surface brightness profile with a radial binning size of  $1''$  within  $10''$  for the *HST* I-band image and compared to the 2MASS surface brightness profile. We found that with a Gaussian kernel of  $2''.5$  FWHM, the smoothed *HST* I-band surface brightness profile matches the 2MASS profile moderately well. The deviations between the two profiles are at most 17% at all radii which are smaller than the conservative 50% uncertainty of the CV/AB contribution we considered in this paper (see below). The unsmoothed *HST* I-band image was then scaled with the same factor as the smoothed *HST* image and was used to estimate the intrinsic K-band surface brightness. With this correction, the flux within the central  $1''$  is higher than the 2MASS estimate by about a factor of two.

To model the X-ray spectrum of the CV/AB component, we fitted the unresolved X-ray emission of the dwarf elliptical galaxy M32, which is believed to be hot gas-free (Revnivtsev et al. 2007; Boroson et al. 2011). Using an absorbed thermal + power law [PHABS\*(APEC+POWERLAW)] model fitted to archival

*Chandra* data, the best-fit temperature was  $T_{\text{CV/AB}} = 0.76_{-0.06}^{+0.07}$  keV and the power law index was  $\Gamma_{\text{CV/AB}} = 1.92_{-0.11}^{+0.07}$ . The CV/AB normalizations of each annulus were determined by the  $L_X$ – $L_K$  scaling relation derived from M32. We investigated the systematic uncertainties by varying the CV/AB normalizations by  $\pm 50\%$ , comparable to the galaxy by galaxy variation of this component (Appendix A). This only changed the measured gas properties slightly within  $\sim 10''$ . All of the systematic uncertainties are smaller than the statistical uncertainties.

The eight observations in 2012 were observed in three different periods (two observations between January 18–January 23, three observations between January 26–February 5, and three observations between April 4–April 7). For each period, the pointings and roll angles of the observations are nearly identical. Therefore, we merged the spectra for observations taken in each period using the CIAO `specextract` script. The three merged spectra of each extraction region in the 0.5–6.0 keV energy range were fitted jointly to the three component absorbed (PHABS) model – a thermal (APEC) model for the gas, a power law (POWERLAW) with a slope of 1.6 for the unresolved LMXBs, and a combination of thermal + power law (APEC + POWERLAW) model for the CV/ABs. We fixed the absorption at the Galactic value of  $N_{\text{H}} = 4.32 \times 10^{20}$  cm $^{-2}$  (Dickey & Lockman 1990). The systematic uncertainty introduced by  $N_{\text{H}}$  is not significant (Appendix A). We fitted the temperature of the thermal gas component. The normalizations of the LMXB component were allowed to vary in the three merged spectra to account for possible variability. For the thermal gas component, when the three normalizations are untied in the joint fitting, they are within the uncertainties of each other. Moreover, the ccd responses did not change much during the observations and the extended hot gas should not be time varying. Therefore, we tied the hot gas normalizations in the fitting. The metallicity was fixed to the solar value using the `wilm` abundance table (Wilms et al. 2000) and the systematic uncertainties of this assumption are discussed in Appendix A. In brief, thawing the metallicity only introduces a small systematic bias in hot gas temperature compared to the statistical uncertainty and increases the gas normalizations by a factor of four to five, and the derived gas density only increases by a factor of two without affecting the density slope (Appendix A). None of our conclusions are sensitive to the adopted metallicity. Unless otherwise specified, all the spectra were fitted using the c-statistic.

### 3. SPATIALLY EXTENDED EMISSION IN THE BONDI REGION AND X-RAY LIMITS OF THE WEAK AGN

Recent radio observations have detected a point source at the center of NGC 3115 with a luminosity of  $L_{8.5\text{GHz}} = 3.1 \times 10^{35}$  erg s $^{-1}$ , suggesting nuclear activity of the supermassive black hole (Wrobel & Nyland 2012). It is important to constrain the luminosity of a potential weak AGN in X-ray, either in understanding the radiative process around the vicinity of the black hole or the potential contamination to extended emission of larger scale thermal hot gas. Earlier studies suggested a point-like source at the center of NGC 3115 and measured an X-ray lu-

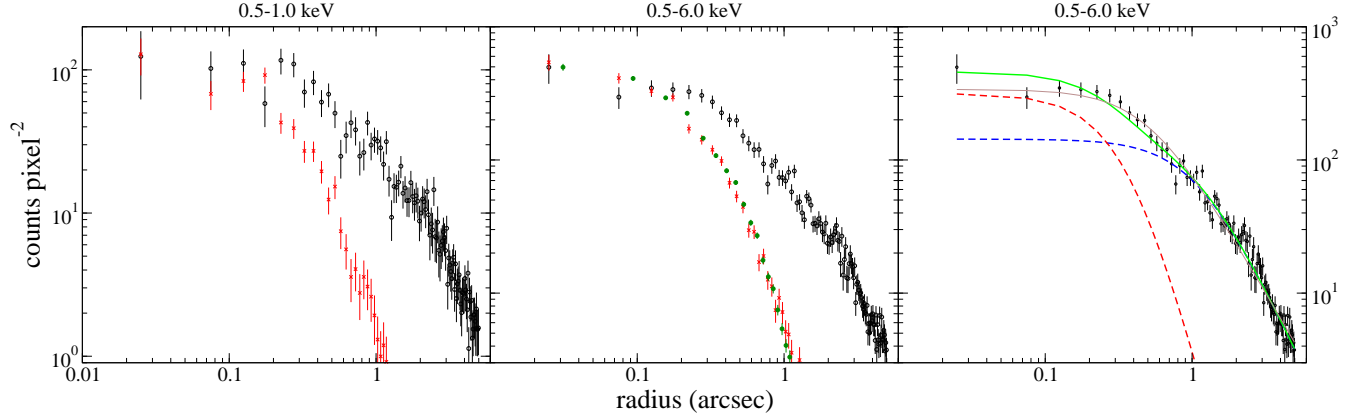


FIG. 2.— Left panel: Surface brightness profiles of the unresolved diffuse emission (black open circles) and a nearby point source  $6''$  away from the center (red crosses) in 0.5–1.0 keV. The point source profile was normalized to the photon counts of the unresolved diffuse profile within  $0''.2$ . This point source is used as the PSF template. Middle panel: Similar as the left panel but in 0.5–6.0 keV. The green solid circle data are from another very bright point source about  $30''$  from the galaxy center. The sum of the two-component (Moffat+Moffat) model is shown in thick solid green, with the individual components of the point source (red dashed) and extended source (blue dashed) shown in dashed lines (See Appendix B below). The single Moffat model is shown as a thin solid brown line. All the error bars in this figure are at the  $1\sigma$  confidence level.

minosity up to about  $4 \times 10^{38} \text{ erg s}^{-1}$  (e.g., Ho 2009; Boroson et al. 2011). Such a high luminosity would explain all the X-ray emission within the central  $1''$  region (although it would hardly be able to contaminate the Bondi region between  $\sim 1''$  and  $5''$  in radius). However, W11 and Miller et al. (2012) argued that any point source emission should be significantly weaker due to the blending of extended emission. W11 provided an upper limit of  $10^{38} \text{ erg s}^{-1}$  for any central point source. In this section, we quantify the extended emission within the Bondi region and provide stricter (while still conservative) limits on the central AGN.

Figure 2 shows the surface brightness profile of the central  $5''$  region and also the normalized profile of a nearby point source. Using other nearby sources gives consistent point source profiles. This figure strongly suggests that the X-ray emission is extended beyond a fraction of an arcsec, with no strong evidence of a central point source. The X-ray emission within the central  $1''$  in radius varied  $\lesssim 2\sigma$  in four different energy bands (0.5–1.0, 1.0–2.0, 2.0–6.0, and 0.5–6.0 keV) in all the eleven observations, showing no evidence of a varying central point source. Spectral analysis suggests that hot gas contributes about half of the soft emission (0.5–1.0 keV) at  $1\text{--}2''$  and is the dominant component beyond that (Figure 5 below), and therefore the left panel of Figure 2 indicates a clearly extended hot gas component beyond sub-arcsec scale.

By modeling the spatial distribution of the X-ray emission within  $5''$  with a two-component model (a point source component and an extended diffuse component; Appendix B), we found that the conservative upper limit of the X-ray luminosity of the AGN is  $L_{X,\text{AGN}} < 4.4 (1.1) \times 10^{37} \text{ erg s}^{-1}$  in 0.5–6.0 (0.5–1.0) keV. This is about two to nine times lower than the quoted detection or upper limits determined recently (e.g., Ho 2009; Boroson et al. 2011; W11; Miller et al. 2012). We determined the upper limit of the Eddington fraction to be  $L_{X,\text{AGN}}/L_{\text{Edd}} < 3.5 \times 10^{-10} (10^9 M_{\odot}/M_{\text{BH}})$ , making it one of the most under-luminous AGNs (Ho 2008). Therefore, the accretion of the NGC 3115 black hole is ex-

pected to be in the hot mode with an expected temperature profile close to the virial temperature of the system and increasing toward the center. We also found that the AGN at most contributes  $\sim 30\%$  to the X-ray emission within a radius of  $1''$  in 0.5–6.0 keV. Such a systematic uncertainty will not affect our results of the hot gas profiles qualitatively (Appendix B). Therefore, we ignore the AGN contribution in our data analysis.

#### 4. SPATIALLY RESOLVED HOT GAS PROPERTIES

##### 4.1. Temperature Profile

###### 4.1.1. Single temperature model

We model the projected spectra of the diffuse gas component with a single temperature optically thin thermal plasma model (APEC) described in Section 2.3. The projected temperature profile is shown in the upper panel of Figure 3. It is clear that the projected temperature is around 0.3 keV in the outer region and increases sharply to about 0.7 keV within about  $5''$ . Within the inner  $2''$  or  $3''$ , the new data now strongly suggest that the projected temperature drops at the center, indicating that there is significant soft emission near the center. Previous analysis of the moderate length 2001+2010 *Chandra* data by W11 suggested an increase in best-fit projected temperature toward the center, although the uncertainty was too large to be conclusive. Such a simple interpretation of a monotonic increase in projected temperature is no longer valid. We also noticed that a single temperature fit to the projected temperature within the inner  $\sim 3''$  is no longer adequate. In Section 4.1.2 below, we present two-temperature fitting results to the data.

###### 4.1.2. Two-temperature model

Single temperature fitting to the projected spectra within the inner  $3''$  suggests a central drop in temperature. However, a single temperature model may not be sufficient to characterize the projected spectra; at the very least the spectra should consist of gas at different temperatures due to projection effects of gas

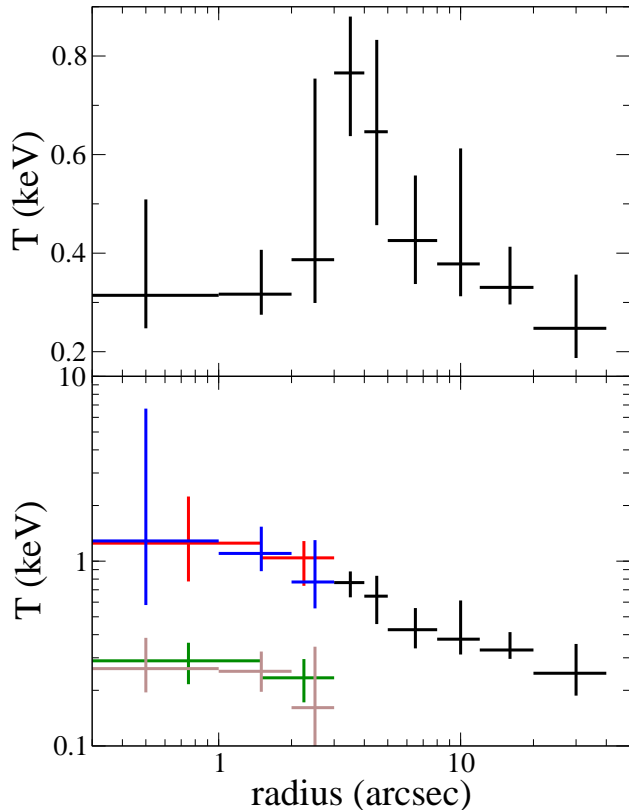


FIG. 3.— Upper panel: Temperature profile using a single temperature model. Lower panel: Temperature profile using a two-component model within  $3''$  with color data points representing each temperature component. The corresponding temperatures of the hotter (red/blue) and cooler (green/brown) components of the two-temperature model represent two different radial binning schemes. There is no evidence of two-(or multi-)temperature structure beyond  $3''$ , and the black data points beyond  $3''$  are the same single temperature shown in the upper panel. For both panels, vertical error bars are at the 90% confidence level and horizontal bars indicate the radial binning size.

at larger radii. Motivated by the expected central rise in temperature for radiatively inefficient accretion flows (RIAFs) accreting in hot modes (e.g., Narayan & Yi 1994; Fabian & Rees 1995; Brighenti & Mathews 1999; Narayan & McClintock 2008; Guo & Mathews 2013) and evidence of central temperature peaks  $\lesssim 300$  pc from the galactic nuclei in a few early-type galaxies (Pellegrini et al. 2003; Humphrey et al. 2008; Pellegrini et al. 2012), we searched for possible evidence of a hot thermal component potentially hidden in a multi-temperature structure within the central  $3''$ . We first examined the spectra with different binning sizes including or removing structures within  $3''$ . We also combined all the different observations taken in 2012 to create a single spectrum in each extraction region, so that the combined spectra have enough counts for visual inspection. This also allows us to group the spectra with a minimum of 25 counts per spectral bin to use chi-squared or F-statistics. We found that while a single temperature model generally gives a good enough fit “globally” ( $\chi^2_\nu \approx 1$ ) for most spectra, there is a notable systematic excess of emission at about 1 keV. An example of a spectrum in an annular region of  $1''$ – $3''$  is

shown in Figure 4. The best-fit temperature of a single temperature model is  $0.37^{+0.11}_{-0.06}$  keV with  $\chi^2 = 75.9$  and 80 degree of freedom. When we added one more thermal component (an APEC model with the same abundance and redshift as the first thermal component), this two-temperature model gave best-fit temperatures of  $1.23^{+0.25}_{-0.21}$  and  $0.29^{+0.05}_{-0.05}$  keV with  $\chi^2 = 53.6$  and 78 degree of freedom. The lower panel of Figure 3 shows the spectrum of the two-temperature model. A simple F-test with the F-statistic of 16.3 and probability of  $1.26 \times 10^{-6}$  strongly suggests that the second component is needed. A more formal test for an additional component was also performed by simulating 1000 spectra with the single temperature model and then comparing the likelihood ratio of the single temperature model with respect to the two-temperature model (likelihood ratio test in XSPEC). We found that all 1000 of the simulated likelihood ratios are smaller than the observed ratio, strongly suggesting that the two-temperature model is preferred. We performed a similar likelihood ratio test to determine whether the extra component is a narrow single line emission or a broader thermal component by simulating 1000 spectra with an extra gaussian model in XSPEC. The line width was fixed to zero. We found that 99.2% of the simulated likelihood ratios of the single temperature + gaussian model with respect to the two-temperature model are smaller than the observed ratio, again, strongly favoring the two-temperature model. We conclude that there is evidence of a hotter thermal component with temperature  $\gtrsim 1$  keV within the central  $3''$  region.

It is possible that there is a wider distribution of temperature structure along the line of sight. Unfortunately, the statistics of our data do not allow us to test beyond a two-temperature model. It is also known that a multi-temperature structure is difficult to be quantified from the data (e.g., Kaastra et al. 2008; Gayley 2013). Here, we simply characterize the thermal component within  $3''$  with a two-temperature model. This two-temperature model at least may be able to characterize the rough lower and upper limits of the temperature distribution. Temperature profiles of the two-temperature model are shown in the lower panel of Figure 3. The fittings were performed by joint-fitting different observations as described in Section 2.3 rather than fitting the combined spectra. Different colors represent different spatial binning. It is interesting that the hotter temperature rises all the way toward the center, consistent with most hot accretion models. Considering the hotter component within  $3''$  and the single temperature profile beyond that, fitting the projected temperature profile to a power law gives  $T \propto r^{-[0.44^{+0.29}_{-0.33}]}$  (90% confidence) for  $r < 5''$  and  $T \propto r^{-[0.34^{+0.25}_{-0.25}]}$  for  $5'' < r < 40''$ . Ignoring the central  $1''$  region gives essentially the same results. It is also interesting that the lower temperature of the two-temperature model is consistent with the low temperature of  $\sim 0.3$  keV outside the Bondi radius.

Since it is quite certain that there are at least two (or multiple) temperature structures within about  $3''$ , we also tested whether there is any evidence of significant two-temperature structure beyond  $3''$ . Between  $3''$  and  $5''$ , the best-fit temperatures and normalizations of the hotter component are consistent with a single tempera-

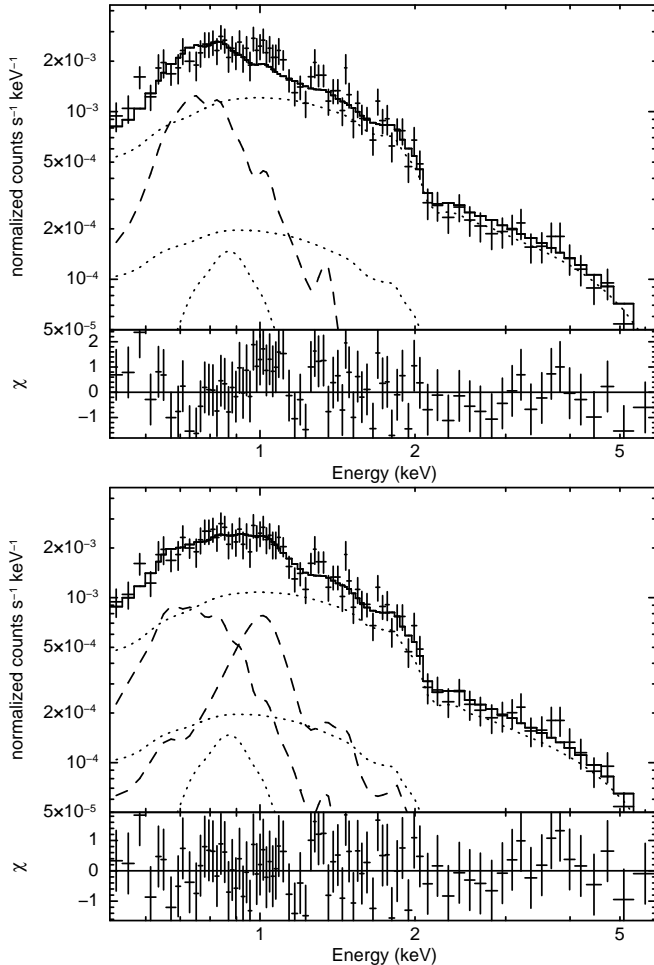


FIG. 4.— Upper panel: Single temperature fit to the spectrum in the  $1''$ – $3''$  annular region. The dashed line is the thermal (APEC) component. The top dotted line is the LMXB component. The two lower dotted lines are the CV/AB component. The solid line is the sum of all the components. A clear residual can be seen at around 1 keV. Lower panel: Similar to the upper panel but with the extra thermal (APEC) component of the two-temperature fit labeled with a second dashed line. All the error bars in this figure are at  $1\sigma$  confidence level.

ture fit; the best-fit lower temperature is consistent with zero, which is unphysically low and the flux (0.5–2.0 keV) of the soft thermal component is less than 10% of the hot component. Beyond  $5''$ , either the higher and lower temperatures are consistent with each other within 90% confidence, or the best-fit temperatures are more sensitive to systematic uncertainties. The best-fit temperatures ( $\sim 0.3$  keV) and normalizations of the cooler component are consistent with single temperature fits. The cooler component dominates over the hot component by a factor of about two to four in normalization. Performing additional tests by tying the higher (and lower) temperature of a few radial bins together does not change the conclusion. We conclude that a single temperature model is sufficient to approximate the thermal structure of the hot gas beyond  $3''$ .

#### 4.2. Surface Brightness Profiles

The surface brightness profiles for the hot gas, the CV/AB, and the unresolved LMXB components are shown in Figure 5. Unlike the surface brightness profiles in W11 which assume all the emission above 2 keV

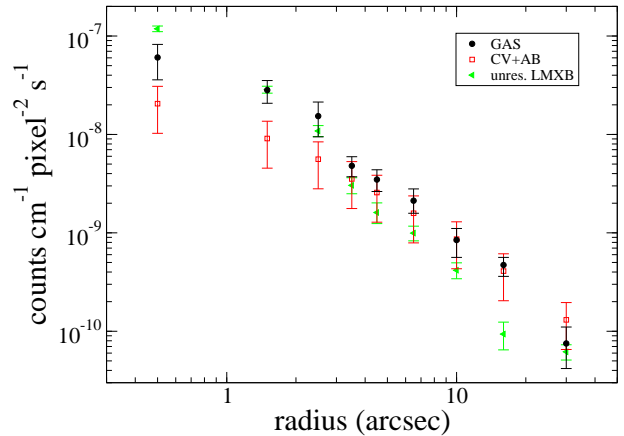


FIG. 5.— Surface brightness profiles for the hot gas (black circles), CV/AB (red squares), and LMXB (green triangles) components in the 0.5–1.0 keV band for NGC 3115. One pixel equals  $0''.492$ . The error bars for the hot gas and LMXB are at the 90% confidence level. The error bars for the CV/AB component are the conservative uncertainties of  $\pm 50\%$  we assumed in addressing the systematic uncertainties.

is contributed by the LMXBs, in this paper, the surface brightness of the hot gas and unresolved LMXB were calculated from the best-fit models spectroscopically. This self-consistently takes into account the uncertainties in the hot gas and LMXB contributions. We use a single temperature model for the hot gas in this plot. In the central region where the gas is multi-temperature, this single temperature model, which has a low temperature of  $\sim 0.3$  keV near the center (Section 4.1.1), should be able to take into account most of the gas emission of the hot gas in the 0.5–1 keV band. Using a two-temperature model gives essentially the same result, but gives larger uncertainties.

The hot gas is robustly detected within  $\sim 20''$ – $40''$ . Hot gas is the dominant component in this energy band out to  $\sim 10''$ – $20''$ . The CV/AB component is not significant within a few arcsec but becomes significant in the outermost regions. However, varying the CV/AB contributions by  $\pm 50\%$  does not change any of our conclusions qualitatively at all radii and does not significantly change any result quantitatively within a few arcsec (Appendix A).

The distribution of optical light of NGC 3115 is highly elliptical. We have tested whether the thermal X-ray emission deviates from azimuthal symmetry by extracting surface brightness profiles of the hot gas in four 90-degree sectors in NW, NE, SE, and SW directions. We conclude that there is no evidence of azimuthally variation for the single temperature model and the hot component of the two-temperature model, and therefore spherical approximation is adequate for our analysis. However, there is some weak evidence that the cooler component of the two-temperature model is distributed more along the major axis of the galaxy within  $3''$  and this implication is discussed in Section 5.4. Nevertheless, we also present systematic tests by assuming the gas is distributed elliptically as the optical light and as a thick disk in Section 5.1.

### 4.3. Emission Measure and Density Profiles

Figure 6 shows the XSPEC APEC normalization per unit surface area, which is proportional to the emission measure of  $\int n_e^2 dl$ , where  $n_e$  is the electron density and  $l$  is the column length along the line of sight. The single temperature model is shown in black in the upper panel and thick grey in the middle and lower panels. The hotter (cooler) component of the two-temperature model within  $3''$  is shown in color in the middle (lower) panel, with different colors representing different spatial binning. In general, the emission measure of the hotter component is lower than the single temperature model but barely consistent within the error bars while the cooler component is comparable to the single temperature model. This indicates that the hotter gas density may be slightly lower and the cooler gas density may be similar to that determined by a single temperature model (as shown below), but the density profiles should not be too sensitive to these two models (since  $n_e \propto \sqrt{\text{emission measure}}$ ). In the central  $1''.5$ , the uncertainties of the hot component appear to be significantly larger than that of the single temperature model. The large error bar is due to the poor temperature constraint in that region, with a higher temperature upper limit so that the gas normalization is degenerate with the hard emission from, e.g., LMXBs. We also noted that there is a weak AGN in the central  $1''$  which can contribute at most up to 30% of the total emission and can increase the hot component uncertainties. Note that this upper limit is very conservative (see Appendix B).

Within  $3''$ , the soft normalization per unit area decreases with radius (lower panel in Figure 6), suggesting that the cooler component should not be projected emission from a much larger relatively-uniform background structure. The centrally peaked soft normalization per unit area suggests that the cooler component should be located physically inside about 150 pc ( $3''$ ) from the galaxy center (see Section 5 for more detailed discussions).

With the XSPEC APEC normalizations (or emission measure) in each annulus, we can deproject the density profile using the onion peeling method as was done in W11 and also outlined in detail in Kriss et al. (1983) or Wong et al. (2008). In brief, this technique calculates the emission measure of each spherical shell starting from the outermost annulus toward the center, and the emission measure of each subsequent shell is calculated by subtracting the projected emission measure from the outer shells. Unlike W11 who deprojected the density from the surface brightness and assumed a certain spectral shape (or gas temperature), in this work, we directly deprojected the density profile from the spatially resolved emission measure fitted from spectra, and therefore the uncertainties of the spectral shape (or temperature) have been partially taken into account. Note that the deprojected density determined here is effectively the root-mean-squared of the density. If the filling factor is less than one or if the gas is not homogeneous, our deprojected density is overestimated (see also Shcherbakov et al. 2013). Unfortunately, X-ray observation alone cannot determine the filling factor or clumpiness. Theoretical models may provide constraints to these factors.

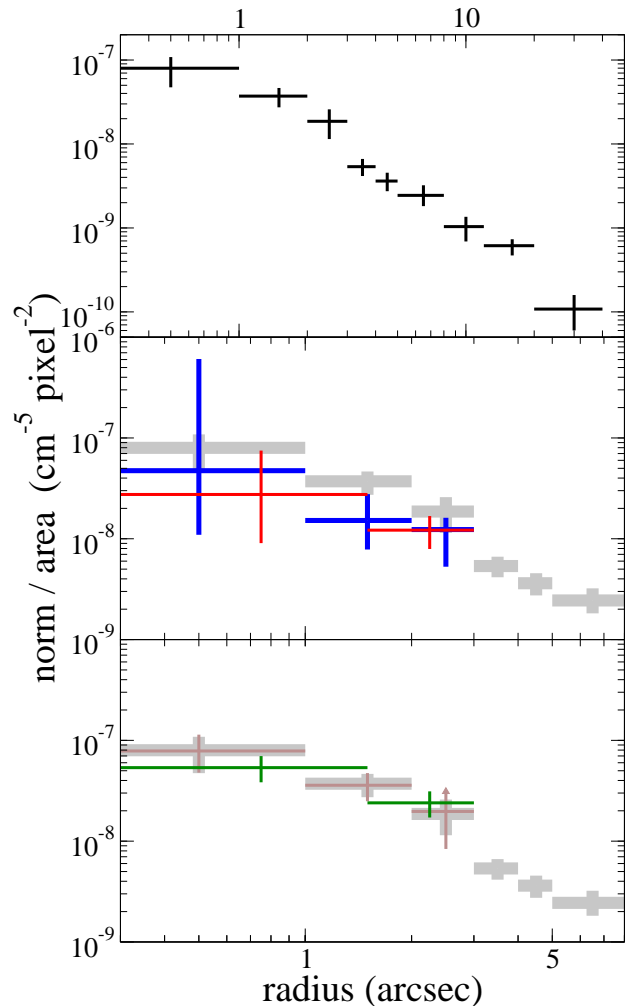


FIG. 6.— Upper panel: APEC normalization per unit area of the single temperature model within  $40''$ . One pixel equals  $0''.492$ . Middle panel: APEC normalization per unit surface area of the hot component of the two-temperature model within  $8''$  are shown in color data points, with different colors for different radial binnings. The thick grey data points are for the same single temperature model shown in the upper panel. Lower panel: Similar to the middle panel but with the low temperature component instead of the hot component. For all panels, vertical error bars are at the 90% confidence level and horizontal bars indicate the radial binning size, with the exception that the upper limit of the data point of the cold component (lower panel) at  $2''.5$  is not well determined and is labeled as a triangle.

The deprojected electron density profiles of the single and two-temperature models are shown in Figure 7. The errors were estimated by running  $10^6$  Monte Carlo simulations. The density profile of the single temperature model (upper panel of Figure 7) is easier to interpret by assuming a single-phase plasma. However, the two-temperature model is more difficult to interpret. It is possible that the two components are in two (or more) distinct phases or the particles can be distributed in a broader than Maxwellian distribution. In any case, the distribution of the two-temperature model cannot be constrained without additional assumptions (e.g., filling factor, gas distribution). Motivated by hints that the colder component may be distributed as a ( $\sim 3''$ ) disk along the major axis of the galaxy and also by the fact



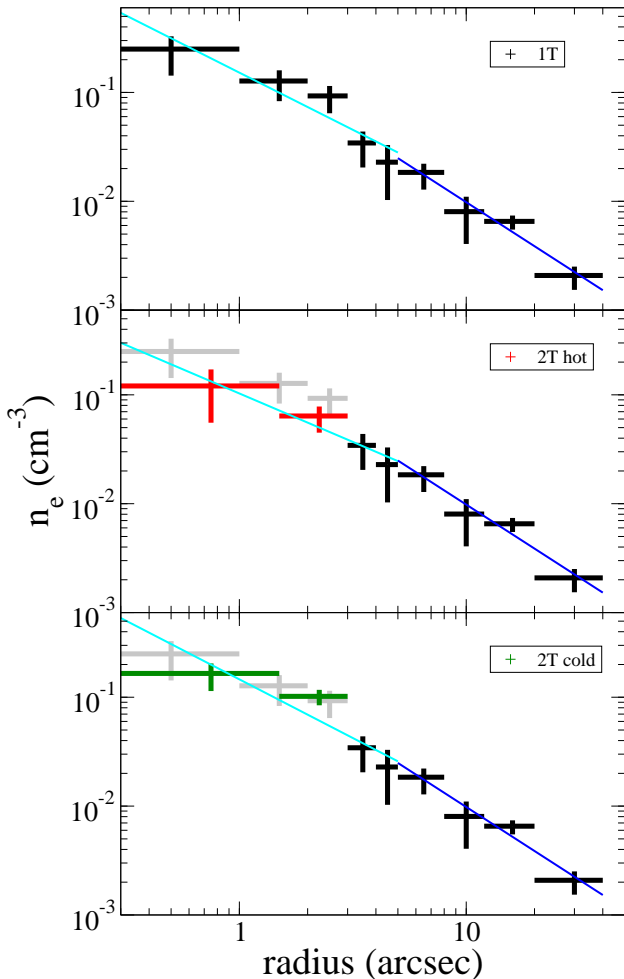


FIG. 7.— Upper panel: Deprojected density profile of the single temperature model (black). The cyan (blue) line has a power law index of 1.05 (1.34) in  $0''$ – $5''$  ( $5''$ – $40''$ ). Middle panel: Deprojected density profile using the hot component of the two-temperature model within  $3''$  (red). Single temperature model (black) were used beyond  $3''$ . The density profile of the single temperature mode within  $3''$  is shown in grey for comparison. The cyan (blue) line has a power law index of 0.89 (1.34) in  $0''$ – $5''$  ( $5''$ – $40''$ ). Lower panel: Similar to the middle panel, but with the hot component replaced by the cold component (green) of the two-temperature model. The cyan (blue) line has a power law index of 1.08 (1.34) in  $0''$ – $5''$  ( $5''$ – $40''$ ). For all panels, vertical error bars are at the 90% confidence level and horizontal bars indicate the radial binning size.

that the hotter component appears to be more spherical, (see Sections 4.2 and 5.4), we assume a simple model that the hotter component characterizes the spherically distributed hot gas in projection within  $3''$  (i.e., assuming a filling factor of 1 for the hotter component). We assume the cold component is concentrated in a small disk-like region that can be ignored when doing the spherical deprojection analysis. The origin of such a cold component is discussed in detail in Section 5. With the two-temperature model within  $3''$ , the emission measure (normalization) cannot be constrained well enough if we thaw the temperatures. In particular, using a narrow spatial binning size of  $1''$  gives too large statistical uncertainties and also the systematic uncertainties in the central

$1''$  can be larger. To improve the constraints, we used a larger spatial bin of  $1.5''$  for deprojection. We fixed all the higher and lower temperatures to their best-fit values and assessed the uncertainties of the normalizations. The deprojected density of the hotter component is shown in the middle panel of Figure 7. As expected, it is slightly lower than the single temperature model. We noted that if we assume the cold component as the spherically distributed gas and ignore the hot component (lower panel of Figure 7), the density profile is closer to the single temperature model. Note that the density profiles under these three different assumptions are remarkably similar, suggesting that these models are measuring similar emission measure that is more sensitive to density than temperature. Note also that if the filling factor is less than one or if the gas is clumpy, the density we measured is biased high.

Fitting the density profile of the hotter component of the two-temperature model within  $5''$  to a power law gives  $\rho \propto r^{-[0.89^{+0.35}_{-0.45}]}$  (90% confidence; note that W11 present  $1\sigma$  confidence). The less physically motivated density profile of the cooler component of the two-temperature models gives  $\rho \propto r^{-[1.08^{+0.31}_{-0.24}]}$  in  $0''$ – $5''$ . The single temperature model gives a power law index of  $1.05^{+0.25}_{-0.25}$  in  $0''$ – $5''$ ,  $0.90^{+0.24}_{-0.30}$  in  $0''$ – $4''$ , and  $0.62^{+0.26}_{-0.38}$  in  $0''$ – $3''$ . The density profile becomes steeper in the  $5''$ – $40''$  outer region, with a power law index of  $1.34^{+0.20}_{-0.25}$ .

## 5. ORIGIN OF THE SOFT EMISSION WITHIN 150 PC

The single temperature model suggests that there is significant soft emission with a characteristic temperature of  $\sim 0.3$  keV within  $\sim 150$  pc ( $3''$ ). The preference for a two-temperature model strongly suggests that there is at least a two (or multiple) temperature structure. We discuss the origin of this soft emission in the following sections. We argue below that it is unlikely that the soft emission emanates from projected gas from larger radii, or from soft stellar sources, but instead is most likely explained by cooler thermal gas located physically within  $\sim 150$  pc.

### 5.1. Insufficient Projected Cooler Gas from the Outer Region

Because the characteristic temperature ( $\sim 0.3$  keV) of the softer emission is very similar to the temperature of the outer region beyond  $\sim 5''$ , it is possible that the softer emission comes from projected gas of the outer regions. However, the surface brightness (or emission measure per unit area) is quite steep in the central  $3''$  (lower panel in Figure 6), which does not appear to come from projected gas of a larger outer region. It would be ideal if we could fit a projection model (such as the XSPEC `projct`, although it has some limitation in the assumed geometry) to test whether projection can account for all the soft emission. Unfortunately, the statistics of the data do not allow us to perform such a test with high confidence. Instead, we performed three conservative tests to quantify the allowed projected soft emission.

We first tested whether the soft emission within  $3''$  can be projected from a spherical distribution of  $\sim 0.3$  keV gas beyond  $5''$ . To maximize the projection effect, we assumed that all gas beyond  $5''$  has a temperature of  $0.3$  keV. This may overestimate the cool gas contribution

as the hot gas temperature between  $\sim 5''$ – $10''$  is slightly hotter and most of the projection should come from this region. We then fitted the gas normalizations in each annulus beyond  $5''$  with the gas temperature fixed to 0.3 keV. By using the onion peeling method (Section 4.3; Kriss et al. (1983); Wong et al. (2008)), the projected gas (flux) contribution to the inner  $3''$  region can be calculated. In the  $1''$ – $3''$  region, we fitted a two-temperature model with the lower temperature fixed to 0.3 keV to estimate the total flux of the cooler component. The inner  $1''$  is ignored due to the potential contamination from a weak AGN. We found that projected gas can only account for 11% of the soft emission in the  $1''$ – $3''$  annulus. Even if the soft emission is at its lower limit of the 90% confidence interval (95% one-sided limit), projected gas can only account for 16% of the soft emission. The statistical uncertainty of the projected gas normalization is of the order of 20–30%, and therefore the uncertainty in projected gas cannot account for the difference.

We then constructed an oblate spheroid model of the gas halo with constant ellipticity which roughly follows the optical light (minor radius/major radius = 0.6; Kormendy & Richstone 1992). Here, we extracted spectra in elliptical annular regions with the radial binning sizes along the major axis equal to our circular annulus sizes. By doing a similar analysis as the spherical model above, we found that projected gas can still at most account for about 22% of the soft emission in the  $1''$ – $3''$  annulus.

Finally, we assume a thick circular disk of uniform gas with thickness of  $6''$  and an outer radius of  $40''$  aligned along the optical major axis. The rotation axis is assumed to be parallel to the plane of the sky along the optical minor axis. We extracted a spectrum from a  $6 \times 80$  arcsec rectangular region aligned along the major axis, with a  $3''$  circular region at the center and point sources excluded. Again, we fitted the APEC normalization of a 0.3 keV gas in this region. The projected gas within the  $3''$  region is proportional to the projected volume. We found that projected gas can only account for 9%–13% of the soft emission within the central  $1''$ – $3''$  annulus. This disk model accounts for a smaller amount of projected gas compared to the ellipsoid model. This may be due to the very bright optical disk in the disk region that overestimates the CV/AB contribution in X-ray and hence underestimates the projected gas. Another reason may be that the gas emission is not disk-like as assumed.

In summary, most of the soft emission within the central  $3''$  cannot be explained by projected emission from a spherical, an oblate spheroid, or a thick disk distribution of cooler gas. Projection may work, e.g., if the outer cooler gas is preferentially distributed toward the line-of-sight of the supermassive black hole, which seems unlikely.

### 5.2. Difficulties of Stripped Cores of Giant Stars

It has been suggested that tidally-stripped cores of giant stars can have very soft spectra ( $E \lesssim$  keV) with relatively large luminosities ( $> 100L_{\odot}$ ) which can last for  $10^3$ – $10^6$  yr around supermassive black holes (e.g., Di Stefano et al. 2001; Davies & King 2005) and could conceivably account for the soft emission inside  $3''$ . The tidal radius of a billion solar mass black hole is  $R_t \approx 1.2R_S(M_*/M_{\odot})^{-1/3}(M_{\text{BH}}/10^9M_{\odot})^{-2/3}(R_*/5R_{\odot})$ ,

where  $R_S$  is the Schwarzschild radius, and  $M_*$  and  $R_*$  are the stellar mass and radius, respectively (MacLeod et al. 2012). Therefore, most main-sequence stars with  $R_* \lesssim 5R_{\odot}$  are directly swallowed by the billion solar mass black hole, but the envelopes of giant stars can be tidally stripped.

First, for the nearest two point-like sources or extended regions located near the major axis at  $1''$ , spectral analysis suggests that their spectra are perfectly consistent with a typical LMXB spectrum with a power-law index of  $1.65 \pm 0.13$ . These weak sources do not affect the spectral analysis of the hot gas and do not provide excess soft emission in the central  $3''$  region. We have removed all the detected point sources within the  $1''$ – $3''$  annular region and there is no indication of any other point source. If the soft emission comes from these soft stripped cores, the luminosity of each source has to be lower than  $\sim 10^{36}$  erg s $^{-1}$  to remain undetected.

Second, the rate of all stars passing through the corresponding tidal radius (including those swallowed and disrupted) of NGC 3115 has been estimated to be about  $\dot{N} \sim 5 \times 10^{-5}$  yr $^{-1}$  (Wang & Merritt 2004), which is roughly consistent with other estimations of giant galaxies with supermassive black holes (e.g., Magorrian & Tremaine 1999; Syer & Ulmer 1999). The fraction of giant stars ( $R_* > 5$ – $10R_{\odot}$ ) passing through the tidal radius is about 5–10% (e.g., MacLeod et al. 2012). Taking the upper limit of 10% gives the tidal stripping rate of giant stars to be  $\dot{N}_G \sim 5 \times 10^{-6}$  yr $^{-1}$ . Even if a stripped core can maintain its luminosity for as long as  $10^6$  yr, there are only about five stripped cores luminous expected at one time around the center of NGC 3115. The total unabsorbed luminosity of the soft component of the two-temperature model in the  $1''$ – $3''$  annular region is  $L_{0.5-2 \text{ keV}} = 2 \pm 0.4 \times 10^{37}$  erg s $^{-1}$ , implying that at least 20 low-luminosity stripped cores are required to account for the soft emission. This is a factor of  $>4$  greater than the expected number of stripped cores at any one time.

Third, from the spatial scale of  $\sim 100$  pc of the soft emission and a typical velocity dispersion of 250 km s $^{-1}$ , these cores would have traveled for 0.4 Myr. If most of the soft emission comes from these stripped cores, the average lifetime of the emission has to be close to the upper limit of the expectation.

In summary, to account for all the soft X-rays with stripped giant cores, each core needs to be less luminous than  $\sim 10^{36}$  erg s $^{-1}$ , the tidal stripping rate of giant stars needs to be higher than the predicted value of a few  $\times 10^{-6}$  yr $^{-1}$ , and the average lifetime of the emission should be longer than a fraction of a Myr. These set very tight and challenging constraints on the properties of the stripped cores to meet in order to explain most of the soft emission seen at the galaxy center.

### 5.3. Multi-temperature Gas?

Given the difficulties of the projected gas and stripped cores scenarios, it is likely that most of the soft emission is physically located within the Bondi region. In fact, it is expected that the interstellar medium (ISM) can be in a multi-temperature phase<sup>7</sup> (e.g., McKee & Ostriker 1977;

<sup>7</sup> It is also known that hot gas in other systems such as galaxy groups or clusters can be multi-temperature (e.g., Buote et al.

Muno et al. 2004; Randall et al. 2006). Simulations have shown that hot gas accreted toward supermassive black holes can be chaotic and has a wide range of temperature within the Bondi radius (Barai et al. 2012; Gaspari et al. 2013; Das & Sharma 2013). Numerical simulations also suggest that thermal instabilities of non-rotating cooling gas occurs when  $t_{\text{cool}}/t_{\text{ff}} \lesssim 10$ , where  $t_{\text{cool}}$  and  $t_{\text{ff}}$  are the cooling time and free fall time scales (Sharma et al. 2011; Gaspari et al. 2013). For NGC 3115,  $t_{\text{cool}}/t_{\text{ff}} \approx 100$  (Shcherbakov et al. 2013), so cooling may not be important to induce thermal instability. However, it may be that there are some regions in NGC 3115 where  $t_{\text{cool}}/t_{\text{ff}} \lesssim 10$  locally and therefore cooling can become important. This cooling gas may also be cooling out of the X-ray emitting hot phase ( $T \gtrsim 0.1$  keV) and therefore only the hotter phase with longer  $t_{\text{cool}}$  is detected (see Figure 5c in Gaspari et al. 2013). It may also be that the gas is not free falling (accretion rate greatly suppressed by, e.g., rotation) and therefore the relevant time scale is the accretion time rather than the free fall time. The accretion rate of any cooling gas out of the X-ray band should, however, not be too high to trigger a powerful AGN at the moment. From a theoretical point of view, such a multi-temperature phase, however, is less likely to be clumpy as clumpiness or fragmentation in accretion flow is more likely to occur with higher accretion rate ( $\eta \dot{M} c^2 / L_{\text{Edd}} \gtrsim 0.02$ , where  $\eta$  is the radiative efficiency; Wang et al. 2012) or larger  $L_{X,\text{AGN}}/L_{\text{Edd}} \sim 0.01$ , where  $L_{X,\text{AGN}}$  is the AGN luminosity (Barai et al. 2012).

#### 5.4. Cooler Gas Resides in a Small Disk?

Hot gas in an early-type galaxy with significant stellar rotational velocity is likely to be rotating to some degree, in particular, if a significant fraction of the hot gas comes from stellar mass loss. For NGC 3115, the total hot gas within  $10R_B$  is about  $5 \times 10^6 M_{\odot}$ . Assuming the specific stellar mass loss rate of  $1.5 \times 10^{-12} \text{ yr}^{-1}$  estimated by Mathews (1989) and a total stellar mass of  $5 \times 10^{10} M_{\odot}$  within  $10 R_B$  (Kormendy & Richstone 1992) implies that only 70 Myr is needed to build up the hot gas from stellar mass loss, which is much shorter than the expected age of an early-type galaxy (on the order of 10 Gyr). Therefore, we expect the angular momentum of the hot gas in NGC 3115 to be comparable to the stellar component. In fact, X-ray observations and numerical simulations suggest that hot gas can be rotating collectively with some rapidly rotating early-type galaxies (e.g., NGC 4649; Brighenti et al. 2009). The implications of rotation of hot gas are discussed briefly in Section 7 below.

As mentioned in Section 4.2, there is some weak evidence that the cooler gas component of the two-temperature model is preferentially located on the major axis while the hot component is more spherically symmetric within the  $3''$  region. Interestingly, there is also a very small and distinct optical thin disk with a radius of about  $3''$  along the major axis of the galaxy as shown with *HST* (Figure 4 in Kormendy et al. 1996 and Figure A8 in Ledo et al. 2010). It is possible that some of the gas can circularize and have enough time to cool toward a small disk region. If this is the case, the cooler gas

can be dynamically uncoupled (or weakly coupled) with the hotter gas halo/flow. Such a geometry can also allow us to deproject the density profile of the more spherical gas by considering only the hot gas component within  $3''$ . A rigorous test of this small cooler disk model is beyond the scope of this paper.

#### 6. NEGLIGIBLE X-RAY CONTRIBUTION FROM RAPIDLY SPUN-UP STARS

Sazonov et al. (2012) suggest that late-type main-sequence stars spun-up in dense environments can contribute significantly to the X-ray emission in the Bondi region of Sgr A\*, although recent *Chandra* observations have already ruled out such a possibility at Sgr A\* (Wang et al. 2013).

In our spectral modeling, we have modeled the X-ray emission contributed from the stellar component (namely CV/AB) by using the  $L_X-L_K$  relation (Section 2). On average, this should have taken into account most of the X-ray emission from all types of stellar components, within the uncertainty of the  $L_X-L_K$  scaling relation. However, it has been suggested that the rapidly spun-up stars can dominate the X-ray emission over all other stellar components in dense environments such as the Galactic nucleus. It is therefore important to know how much of the X-ray emission within the central region (e.g., the central  $1''$ ) of NGC 3115 can be contributed by the these rapidly spun-up stars.

First, Sazonov et al. (2012) estimated that the effect of X-ray emission induced by tidal spin-up is limited to a dense region where tidal spin-up is effective. This corresponds to the central region with high stellar density  $\gtrsim 2-3 \times 10^7 M_{\odot} \text{ pc}^{-3}$  within a distance  $\sim 0.06$  pc from Sgr A\*. In NGC 3115, the stellar density peak is about  $2 \times 10^6 M_{\odot} \text{ pc}^{-3}$  (Emsellem et al. 1999) which is much smaller than the condition in Sgr A\*. Therefore, tidal spin-up should not be important in the nuclear region of NGC 3115.

Second, the X-ray luminosity in 2–8 keV within  $\sim 0.06$  pc from Sgr A\* is  $\sim 10^{33} \text{ erg s}^{-1}$ . The total stellar mass (including non-spun-up stars) within that radius is estimated to be  $6-8 \times 10^4 M_{\odot}$  (Sazonov et al. 2012). Assuming all of the X-ray emission comes from rapidly spun-up stars, the luminosity per unit mass is at most  $1.7 \times 10^{28} \text{ erg s}^{-1} M_{\odot}^{-1}$ . For NGC 3115, the total stellar mass of the nuclear cluster of NGC 3115 with a stellar density peak of  $2 \times 10^6 M_{\odot} \text{ pc}^{-3}$  and a characteristic radius of  $\sim 2$  pc (Emsellem et al. 1999; Kormendy et al. 1996) is  $\sim 7 \times 10^7 M_{\odot}$ . The lower density regions beyond  $\sim 2$  pc should not have significant number of these spun-up stars. Even if we assume that all the late-type main-sequence stars of the nuclear cluster in NGC 3115 can be spun-up to a similar degree as to those around Sgr A\*, the total X-ray luminosity from these spun-up stars in the nuclear cluster can only be about  $10^{36} \text{ erg s}^{-1}$  in 2–8 keV. Using the spectral model described in Sazonov et al. (2012), we converted the luminosity to the 0.5–2 keV band and it is about  $4 \times 10^{35} \text{ erg s}^{-1}$ , which is at least 50 times lower than the gas luminosity we determined within  $1''$  ( $\sim 50$  pc). To account for all the gas luminosity we measured, the X-ray emission efficiency in NGC 3115 would need to be 50 times larger than that around Sgr A\*. Increasing X-ray emission efficiency by a higher spin-up efficiency

in NGC 3115 is unlikely given the lower stellar density at the center of NGC 3115. Therefore, we conclude that spun-up stars are very unlikely to contribute significantly to the X-ray emission in the Bondi region of NGC 3115.

## 7. IMPLICATIONS FOR ACCRETION MODELS

### 7.1. Influence of the Black Hole

Since the dynamical time scale (sound crossing time) is much shorter than the heating, cooling, or conduction time scales near the Bondi radius (Shcherbakov et al. 2013), in the absence of a (supermassive) black hole, the hot gas should be in hydrostatic equilibrium (HSE) with the galactic potential. We tested whether the measured gas density profile is consistent with hot gas in HSE with the galactic potential without a black hole. We model the hydrostatic gas density profile with the total stellar mass profile described in Shcherbakov et al. (2013). The gas mass is neglected as it is much smaller than the stellar mass, and dark matter is also neglected near the Bondi scale in which we are interested. Figure 8 shows the density predicted by the adiabatic model (thick dashed green) and the isothermal model (dot-dot-dashed red). Note that the measured temperature profile of the cooler component of the two-temperature model is perhaps fairly isothermal and the entropy of the hotter component is close to adiabatic<sup>8</sup> justify the comparison to isothermal and adiabatic HSE models. The HSE profiles, as well as the measured data points, are normalized at 5". A single temperature model of the hot gas, which roughly corresponds to the cooler thermal component of the two-temperature model, is not consistent with the two HSE models, even accounting for the possible normalization (density) uncertainty at 5" (thin dashed green). The hot component of the two-temperature model is not consistent with the isothermal HSE model, as expected from the rising temperature toward the center. It is also not very consistent with the adiabatic HSE model. If we account for the normalization (density) uncertainty by shifting up the adiabatic HSE model by the density uncertainty at 5" (thin dashed green), the inner region is more consistent with the adiabatic HSE model but the density in the region between 5" and 10" deviates more from the model.

The classical Bondi flow model without a galactic potential is shown as a dot-dashed orange line in Figure 8. Compared to the HSE models, the inner most region fits better but is still inconsistent with the data. There is a large discrepancy beyond  $\sim 8''$ , due to the ignorance of the galactic potential in this model. In fact, the total enclosed stellar mass at about  $1''$ – $2''$  is reaching  $\sim 10^9 M_\odot$ , and therefore the galactic potential has to be taken into account self-consistently. We demonstrate the effect of the galactic potential with a Bondi-like modeling including the galactic potential with the flow rate fixed to be the classical Bondi accretion rate (solid blue line in Figure 8). A more realistic model with stellar feedback and conduction is presented in Shcherbakov et al. (2013), although the existence of a billion solar mass black hole has to be an assumed prior in that model. Our model here

<sup>8</sup> Entropy can be usefully quantified as  $T/n_e^{2/3}$ . Since the measured temperature of the hotter component scales with radius as  $T \sim r^{-a}$ , with  $a \lesssim 1$ , and  $n_e \sim r^{-1}$ , the entropy profile is therefore close to adiabatic.

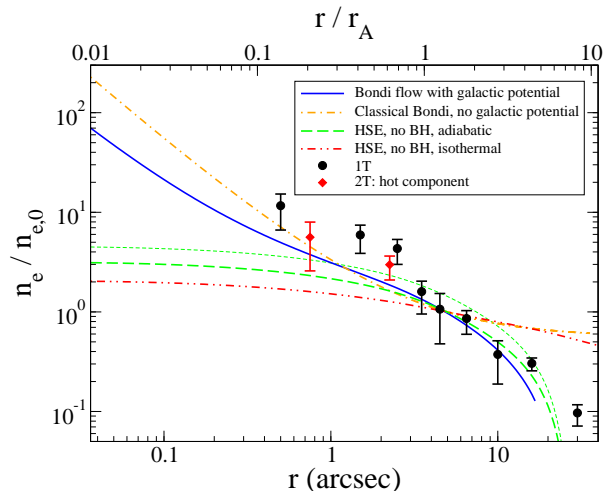


FIG. 8.— Density profiles of different models. Bondi-like flow in a galactic potential is shown in solid blue. The classical Bondi solution with the black hole potential only is shown in dot-dashed orange. Hydrostatic models without a black hole are shown in thick dashed green and dot-dot-dashed red for adiabatic and isothermal models, respectively. The density profiles are normalized to density  $n_{e,0}$  at a characteristic radius of  $5''$ . The characteristic radius here is defined as  $r_A \equiv 2GM_{1.5}/c_{0.3}^2$ , where  $M_{1.5} \equiv 1.5 \times 10^9 M_\odot$  and  $c_{0.3}$  is the adiabatic sound speed at 0.3 keV. Density profiles measured from the X-ray data are shown as black circles for the single temperature model and as red diamonds for the hot component of the two-temperature model. The error bars are at the 90% confidence level. Note that the error bars of the two-temperature model should be underestimated because of the uncertainties in temperature. Thin dashed green line is the adiabatic HSE model normalized at the measured upper density limit at  $5''$ .

is more consistent with the data in a larger radial range ( $\lesssim 10''$ ) compared to the HSE and the classical Bondi models. In particular, the model agrees quite well with the hot component of the two-temperature, although the uncertainties of the gas density are underestimated because the uncertainties in temperature of the hotter component were not taken into account (Section 4.3). There is still a large discrepancy between the single temperature model (or the cooler component of the two-temperature model).

Our data suggest that adiabatic or isothermal HSE with the absence of a black hole is ruled out. Rotation of hot gas would give an even flatter density profile. The short dynamical time scale argues against non-HSE with the absence of a black hole. The X-ray data alone suggest that the rise in density toward the Bondi radius is more likely due to the gravitational influence of the supermassive black hole, in which the existence is supported by optical observations (Kormendy & Richstone 1992; Kormendy et al. 1996; Emsellem et al. 1999). Note that a similar technique has also been used to detect a massive black hole in the giant elliptical galaxies NGC 4649 with its Bondi radius of  $\sim 1''$  using X-ray data alone (Humphrey et al. 2008). The gravitational influence of the black hole should, however, compress and heat the hot gas at the center. It is puzzling that the single temperature profile shows a decrease in temperature toward the center. As discussed in Sections 4.1.2, 4.3, 4.2, and 5, the softer component might be located more in a

small disk region and the hotter component of the two-temperature model might be the more spherical accretion/outflow component.

The X-ray data alone support that we are witnessing the onset of an accretion (out)flow due to the gravitational influence of the billion solar mass supermassive black hole. The hot gas is likely to be in transition from the ambient gas in the galactic potential near the Bondi radius. Within  $\sim 1''$ – $2''$ , the galactic potential becomes negligible. Combining detailed theoretical modeling (e.g., Shcherbakov et al. 2013) together with deeper radio observations to constrain the plasma properties in the vicinity of the black hole should allow us to distinguish among different accretion models.

Our results also suggest that in all other hot accretion flows, the transition regions (around the Bondi scale) connecting the ambient gas and the asymptotic flow near the black hole should contribute significant X-ray emission. Theoretical models should take into account such a transition region in order to probe the inner most accretion region (e.g., Quataert & Narayan 2000).

### 7.2. Self-similar Arguments

Recently, Yuan et al. (2012) performed simulations of hot accretion flows which span a much larger dynamical range compared to many previous simulations. They found that all their numerical simulations show single power law self-similar profiles spanning close to the Bondi radius down to  $1$ – $10R_S$ . Such results agree with many other previous simulations. In particular, they found that all radial profiles scale with similar power law indexes regardless of viscosity, magnetic field, or initial conditions. For instance, their simulated density profile scales as  $\rho \propto r^{-3/2+p}$ , with  $p = 0.65$ – $0.85$  from their simulations<sup>9</sup>, which is consistent with our measured density profile of  $\rho \propto r^{-[0.62^{+0.26}_{-0.38}]}$  within  $3''$  (141 pc) for our single temperature model and close to  $\rho \propto r^{-1}$  for a wider range of radii and for the hotter component of the two-temperature model. Hot gas near the Bondi radius may still be in transition from the ambient ISM to the accretion flow, and therefore the density slope near the Bondi radius may not reach the asymptotic value of the accretion flow (e.g., Bondi 1952; Quataert 2002). For accretion flow in a galactic potential, the transition may be smoother than the accretion flow in a uniform ambient ISM (e.g., Quataert & Narayan 2000). If the asymptotic density profile toward the black hole is close to the predictions by Yuan et al. (2012), the density profile of NGC 3115 may be more smoothly in transition from the region around the Bondi radius all the way toward the event horizon, and therefore a single power-law in density between  $\sim R_S$  and  $\sim R_B$  may be applicable.

For comparison, Wang et al. (2013) recently estimated a density power law index of one for Sgr A\*, which generally agrees with NGC 3115. Since the spectrum in Sgr A\* is not spatially resolved, they had to assume a temperature profile of the form  $T \propto r^{-1}$  to estimate the density profile. Similar to NGC 3115, the flow in Sgr A\* may also be in transition near its Bondi radius so that the asymptotic  $T \propto r^{-1}$  behavior may not be applicable.

A flatter temperature profile would give a flatter density profile which is more consistent with the density profile of our single temperature model in NGC 3115.

At about  $1''$  (47 pc), the electron density of the single temperature model is  $0.15 \text{ cm}^{-3}$ . While there are larger uncertainties in the two-temperature model and the metallicity, the density should not be off by more than an order of magnitude. The accretion rate at  $1''$  (47 pc) is then estimated to be  $\dot{M}_{\text{acc}}(47 \text{ pc}) = 4\pi\lambda R^2 \rho c_s = 9 \times 10^{-3} M_\odot \text{ yr}^{-1}$ , where  $\lambda = 0.25$  and  $\gamma = 5/3$  for an adiabatic process,  $c_s = \sqrt{\gamma k_B T / \mu m_p}$  is the adiabatic sound speed,  $\mu = 0.63$  is the mean molecular weight, and  $T = 0.3 \text{ keV}$  is assumed. The uncertainty of  $T$  also will not introduce an error in the accretion rate by more than an order of magnitude.

The mass accretion rate estimated at  $1''$  (47 pc) from the black hole is a factor of a few smaller than the accretion rate of  $(2\text{--}4) \times 10^{-2} M_\odot \text{ yr}^{-1}$  estimated around a larger radius of  $4''$ – $5''$ . This highlights the systematic uncertainty in estimating the accretion rate near or beyond the Bondi radius in other galaxies with unresolved/underresolved Bondi radii. The estimation near  $1''$  (47 pc) is closer to the upper limit of  $2 \times 10^{-3} M_\odot \text{ yr}^{-1}$  we estimated in a more self-consistent model (Shcherbakov et al. 2013).

The upper limit of the X-ray luminosity of the central AGN is  $4.4 \times 10^{37} \text{ erg s}^{-1}$ , which is about six orders of magnitude smaller than the accretion luminosity ( $5 \times 10^{43} \text{ erg s}^{-1}$ ) at  $1''$  if we assume a 10% radiative efficiency. As discussed in W11, this discrepancy can be explained if the accretion rate near the black hole is suppressed as predicted by ADIOS or CDAF models with the scaling relation  $\dot{M} \propto r^p$ . Yuan et al. (2012) found in their simulations that the accretion rate is constant within about  $10R_S$  and the accretion rate scales as  $\dot{M} \propto r^p$  beyond  $10R_S$ , as expected in the ADIOS model. Assuming the accretion rate at  $10R_S$  is suppressed by six orders of magnitude, the scaling relation gives  $p \approx 1.3$  for a billion solar mass black hole. Such a high value of  $p$  is outside the theoretical upper limit of 1 and also larger than most of the simulated results of 0.5–0.7 (Yuan et al. 2012). However, observational uncertainties may bring  $p$  close to one, which is consistent with the latest version of the ADIOS model (Begelman 2012). Such a high  $p = 1$  value suggests a very flat density profile of  $\rho \propto r^{-0.5}$ , consistent with the power law slope of  $0.62^{+0.26}_{-0.38}$  (90% confidence) within  $3''$  (141 pc) for the single temperature model.

It is also likely that other factors are needed to explain the large discrepancy in X-ray luminosity and accretion rate. For example, accretion may be highly suppressed by rotation close to the event horizon of the black hole (Proga & Begelman 2003; Li et al. 2013) and significant outflow can also be generated during the rotational accretion process (Blandford & Begelman 1999; Li et al. 2013), although the suppression can be less effective if the gas viscosity is sufficiently high (Narayan & Fabian 2011). Numerical simulations show that rotation can flatten density and temperature profiles (Brighenti et al. 2009). Stellar feedback should also suppress the accretion as discussed in Hillel & Soker (2013) & Shcherbakov et al. (2013), with the latter authors also

<sup>9</sup> Note the different symbols defined for the scaling relations in Yuan et al. (2012).

including conduction as a possible suppression mechanism. It is also possible that the radiation efficiency can be lower than the 10% canonical value we assumed (Ho 2008).

### 7.3. Feedback Models

The discussion above was based on steady or quasi-steady state flows without feedback. However, the dynamics of hot gas within a Bondi radius is not only governed by the black hole (and the galactic) potential alone. If there is (was) a sudden release of feedback energy from the black hole (recently) as we see in other giant elliptical galaxies, dynamical disturbance will be important (e.g., Fabian 2012; McNamara & Nulsen 2012). Since there is no strong evidence of AGN feedback in NGC 3115 (e.g., strong radio source, jet, or X-ray bubble), we do not consider strong dynamical flow in this paper. For weak AGN such as NGC 3115 or Sgr A\*, other feedback mechanisms such as stellar feedback or conduction can also play important roles (Hillel & Soker 2013; Soker et al. 2013; Shcherbakov et al. 2013). Therefore, resolving the gas profiles within the Bondi radius is only a step further toward the understanding of black hole accretion. Realistic theoretical modeling and simulations should be performed to match observations, and we present our effort by including conduction and stellar feedback in NGC 3115 in our companion paper (Shcherbakov et al. 2013).

## 8. SUMMARY AND CONCLUSIONS

With a temperature of 0.3 keV for the ambient hot gas, the Bondi radius of the supermassive black hole in NGC 3115 is  $R_B = 112\text{--}224$  pc =  $2''.4\text{--}4''.8$  (W11). Radio observations have recently detected a weak AGN with  $L_{8.5\text{GHz}} = 3.1 \times 10^{35}$  erg s $^{-1}$  at the galaxy center (Wrobel & Nyland 2012). We searched for a signature of the AGN in X-ray but we did not find any strong evidence of a central point source. We determined the upper limit of the X-ray luminosity to be  $L_{X,\text{AGN}} = 4.4(1.1) \times 10^{37}$  erg s $^{-1}$  in 0.5–6.0 (0.5–1.0) keV. The Eddington fraction is thus  $L_{X,\text{AGN}}/L_{\text{Edd}} < 3.5 \times 10^{-10} (10^9 M_\odot / M_{\text{BH}})$ , making it one of the most underluminous AGNs (Ho 2008). Therefore, the accretion of the NGC 3115 black hole is expected to be in the hot mode with an expected temperature profile close to the virial temperature of the system and increasing toward the center as  $T \propto r^{-1}$  (see, e.g., Narayan & McClintock 2008, and references therein).

The hot gas component of the X-ray emission within the Bondi radius is clearly extended and is resolved both spatially and spectrally. The hot thermal plasma is robustly detected out to  $\sim 10R_B$  (a few tens of arcsec). We studied accretion-model independent temperature and density profiles within and around the Bondi radius.

The projected temperature of a single temperature model of the ambient hot gas is slowly increasing from the outer region of  $\sim 30''\text{--}40''$  ( $\sim 1.5\text{--}2$  kpc) toward  $5''$  (235 pc), consistent with 0.3 keV. The projected temperature jumps significantly to a higher temperature of  $\sim 0.7$  keV within  $\sim 4''\text{--}5''$ , but then abruptly drops back to  $\sim 0.3$  keV within  $\sim 3''$  (141 pc). This conflicts with the theoretical expectation that the temperature should be rising toward the center, suggesting that there is significant softer emission within a scale of  $\sim 150$  pc (around

the Bondi scale) compared to a simple hot accretion model with a monotonic increase in temperature.

With the high quality Megasecond *Chandra* data, we found evidence that at least a two-temperature model is needed in the inner few arcsec (150 pc). The hotter temperature of the two-temperature model increases toward the center to  $\sim 1$  keV, consistent with predictions from hot accretion models. The softer component, which dominates over the hotter component in emission measure (gas normalization) by a factor of two to four, has a temperature of  $\sim 0.3$  keV. The softer component cannot be accounted for by projection of cooler surrounding gas with a spherically symmetric distribution. Even if we assume the cooler surrounding gas is distributed as a pancake-like ellipsoid roughly following the optical light or a very thick disk structure, this can at most account for about 22% of the softer component in the central  $1''\text{--}3''$ . We argued that the cooler component at the center is indeed physically located in the central  $\sim 150$  pc rather than projected gas from the outer region, unless the distribution of the outer cooler gas preferentially aligns toward the line-of-sight of the supermassive black hole, which is not very likely. Tidally-stripped cores of giant stars near the supermassive black hole may emit soft X-rays (Di Stefano et al. 2001; Davies & King 2005), but it is also unlikely to explain most of the softer X-ray emission.

We argued that the softer component in the central 150 pc more likely comes from diffuse gas which can be in a multi-temperature phase, as supported by recent numerical simulations (e.g., Gaspari et al. 2013). We also noticed some weak evidence that the cooler component is preferentially located along the major axis, resembling a small thin disk seen on an optical *HST* image (Kormendy et al. 1996). The hotter component is more spherically distributed. The cooler component may be circulating and cooling toward a disk region.

Sazonov et al. (2012) suggested that late-type main-sequence stars spun-up in dense environment can contribute significantly to X-ray emission in galactic centers. We argued that it is very unlikely to be the case in NGC 3115.

The density profile of NGC 3115 suggests that hot gas in adiabatic or isothermal HSE with the galactic potential in the absence of a black hole is ruled out. The short dynamical time scale also argues against non-HSE without a black hole. Therefore, we are witnessing the onset of an accretion (out)flow influenced by the strong gravity of the supermassive black hole. It is puzzling, however, that the single temperature profile drops at the center rather than compressionally heated to a higher temperature, although the detected hot gas may be in a multi-temperature phase as mentioned above.

We determined that the density profile is broadly consistent with  $\rho \propto r^{-1}$  within  $5''$  (235 pc) around the Bondi radius for either the single temperature or the two-temperature model. In particular, the density profile flattens to  $\rho \propto r^{-[0.62^{+0.26}_{-0.38}]}$  within  $3''$  (141 pc) for the single temperature model. This is remarkably consistent with the narrow range of power law index of 0.65–0.85 determined from a large number of numerical simulations spanning a very large dynamical radial range (Yuan et al. 2012). Note that the density we determined depends on

the assumed geometry. If the gas is significantly clumpy and/or if the filling factors of two-temperature model are less than one, the density determined is overestimated.

We estimated that the accretion rate at  $1''$  (47 pc) to be  $\dot{M}_{\text{acc}}(47 \text{ pc}) = 9 \times 10^{-3} M_{\odot} \text{ yr}^{-1}$ , which is a factor of a few smaller than the accretion rate determined at a larger radius of  $4''$ – $5''$ . This illustrates the systematic uncertainty in estimating the accretion rate near or beyond the Bondi radius in galaxies for which the Bondi region is not spatially resolved.

Since the upper limit of the X-ray luminosity of the central AGN is about six orders of magnitude smaller than the accretion luminosity, hot gas actually accreted through the event horizon must be highly suppressed by, e.g., outflow, rotational support, and/or stellar feedback. Radiation efficiency may also be much lower than the 10% canonical value.

Future mission like *SMART-X*<sup>10</sup> with an order of magnitude increase in effective area compared to *Chandra* will allow us to collect enough photons to rigorously study the dynamical properties of the accretion flow within the Bondi radius of NGC 3115 (and potentially

M31\*). The sub-arcsec resolution comparable to *Chandra* is essential. On the other hand, combining high angular resolution radio observations by, e.g., the Event Horizon Telescope<sup>11</sup>, to probe the hot gas properties around the very large event horizon ( $2$ – $4 \mu\text{as}$ ) of NGC 3115 should allow us to understand how gas is being accreted from the Bondi radius down to the black hole.

We thank the referee for the comments. We also thank Rosanne Di Stefano, Eric Emsellem, Dacheng Lin, Peter Maksym, William Mathews, Paul Nulsen, Yuanyuan Su, and Feng Yuan for useful discussions. The work is supported by *Chandra* XVP grant GO2-13104X. RVS is supported by NASA Hubble Fellowship grant HST-HF-51298.01. Some of the data presented in this paper were obtained from the Mikulski Archive for Space Telescopes (MAST). STScI is operated by the Association of Universities for Research in Astronomy, Inc., under NASA contract NAS5-26555. Support for MAST for non-HST data is provided by the NASA Office of Space Science via grant NNX09AF08G and by other grants and contracts.

## APPENDIX

### A. SYSTEMATIC UNCERTAINTIES

In Section 4.1.1, we characterized the projected spectrum of the hot gas component by a single temperature model. Although the single temperature model may not be a physically correct model to describe the thermal plasma, it generally gives good fits to characterize the projected spectra. To ensure this single temperature characterization of the projected spectra is robust, we checked against systematic uncertainties in spectral modeling extensively as outlined below.

#### *CV/AB uncertainties*

We modeled the CV/AB contribution in X-ray by assuming the  $L_X$ – $L_K$  scaling relation determined from M32. The galaxy by galaxy variation is about 30% (rms) for 11 nearby early-type galaxies (Bogdán & Gilfanov 2011) and about 30–40% for 3 nearby early-type galaxies studied by Revnivtsev et al. (2008). We varied the CV/AB normalizations by  $\pm 50\%$  which is comparable to these galaxy by galaxy variations and also larger than the statistical uncertainties of about 30% (90% confidence level) in the spectral fitting of M32. Varying the CV/AB normalizations only introduces very small systematic biases to the temperatures or gas normalizations (densities) within  $\sim 10''$  and larger ones beyond that (left column in Figure 9). All of the systematic uncertainties are within the statistical uncertainties (90% confidence).

#### *Unresolved LMXB uncertainties*

The power-law index of the combined spectrum of all the resolved point sources within  $D_{25}$  is  $\Gamma_{\text{LMXB}} = 1.61^{+0.02}_{-0.02}$ , consistent with the value of 1.6 determined in the bulge of M31 (Irwin et al. 2003). We assessed the systematic uncertainties of the power-law index of unresolved LMXBs by changing  $\Gamma_{\text{LMXB}}$  to 1.4 and 1.8 (middle column in Figure 9). Changing the LMXB power-law index to 1.8 only introduces negligible systematic uncertainties of less than 3% in temperature. A power-law index of 1.4 changes the temperature by less than 2% in general, but with a large change of 12% in the  $4''$ – $5''$  bin. These are all well within the 90% confidence of the statistical uncertainties. The normalizations are generally changed by 10–20% and at most by about 40%. This generally leads to density biases of less than 10% and at most by  $\sim 20$ – $30\%$ . All of these are comparable to the statistical uncertainties.

We also examined the systematic uncertainties of the normalizations of the unresolved LMXBs by fixing them to their upper and lower limits (90% confidence) of the nominal fitting (right column in Figure 9). Fixing the LMXB normalizations to their lower limits (solid red) generally lowers the gas temperatures and normalizations (densities), but within the statistical uncertainties. When we fixed the LMXB normalizations to their lower limits (solid green), the temperatures are biased higher, particularly in the outer regions. We noticed that in the seventh and the ninth bins, there are local minima with deviations of c-statistics from the global minimum  $\Delta C < 1$ . The profiles at these local minimums (dashed green lines) are much closer to the nominal profiles. These larger biases in temperatures in the outer regions may be due to the underestimation of the hard photons from LMXBs and therefore the thermal component in the model tries to compensate for the excess hard photons with higher temperatures. The existence of the second minimum indicates the significance of a thermal component that is closer to the nominal model. Nevertheless,

<sup>10</sup> <http://smart-x.cfa.harvard.edu/>

<sup>11</sup> <http://www.eventhorizontelescope.org>

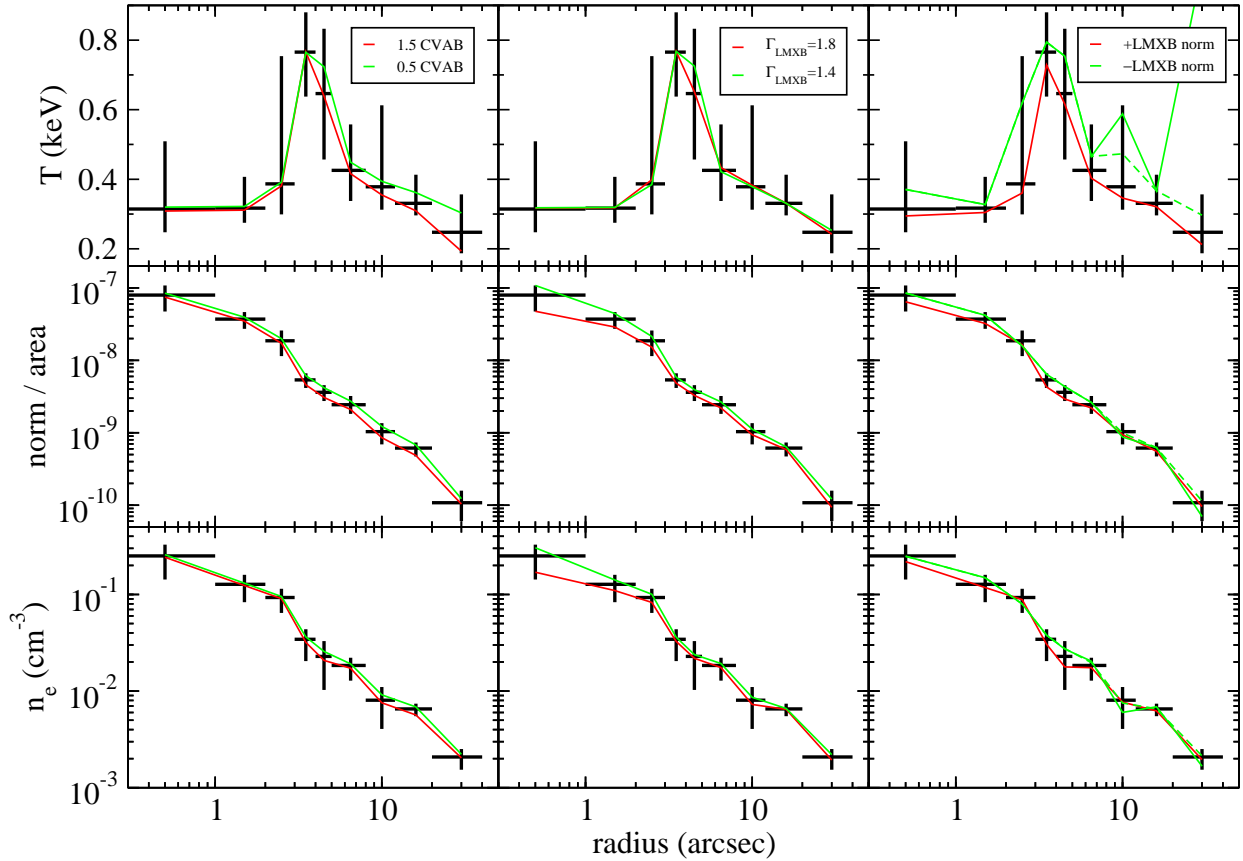


FIG. 9.— Left column: Systematic uncertainties introduced by CV/AB normalizations. The upper panel shows the temperature profiles of the nominal single temperature model (black). Model with CV/AB contribution increased (decreased) by 50% is shown in red (green). The middle panel shows the APEC normalization per unit area ( $\text{cm}^{-5} \text{ pixel}^{-2}$ ) of the nominal single temperature model (black) and models with CV/AB contribution changed by +50% (red) and -50% (green). The lower panel shows the deprojected density profiles of the nominal single temperature model (black) and models with CV/AB contribution changed by +50% (red) and -50% (green). Middle column: Similar as left row, but with the red (green) lines representing a model with LMXB power-law index of  $\Gamma_{\text{LMXB}} = 1.8(1.4)$ . Right column: Similar as left row, but with the red (green) lines representing a model with LMXB normalizations fixed to their upper (lower) limits (90% confidence). Note that there are local minima in c-statistics within the 90% confidence regions for the model with LMXB normalizations fixed to the lower limits, and the profiles corresponding to these local minima are shown as dashed green lines. For all panels, vertical error bars are at the 90% confidence level and horizontal bars indicate the radial binning size.

the gas normalization and density profiles are hardly biased by the systematic uncertainties of the unresolved LMXB normalizations.

#### Hydrogen column density uncertainties

Ideally, the absorption should be fitted from the spectrum, but thawing the absorption gives an unphysically low  $n_{\text{H}}$  of zero, suggesting a degeneracy between  $n_{\text{H}}$  and the hot gas component. Given the generally low  $n_{\text{H}}$  intrinsic to early-type galaxies and also the insignificant amount of total HI (less than a few  $10^7 M_{\odot}$ ) in NGC 3115 (Roberts et al. 1991; Karachentsev et al. 2004; Sage & Welch 2006), we fixed  $n_{\text{H}} = 4.32 \times 10^{20} \text{ cm}^{-2}$  to the Galactic value (Dickey & Lockman 1990). Fitting the  $n_{\text{H}}$  with bright resolved LMXB in NGC 3115 generally gives a higher  $n_{\text{H}}$  by at most 60% but consistent with the Galactic value within  $1\sigma$ – $3\sigma$  in uncertainties. We assessed the systematic uncertainty in absorption by fixing  $n_{\text{H}} = 10 \times 10^{20} \text{ cm}^{-2}$  (left column in Figure 10). Even if the absorption is this high, the temperatures are only slightly biased lower and the gas normalizations (densities) are biased higher to the upper limit of the uncertainties of the nominal model. This does not change our results qualitatively.



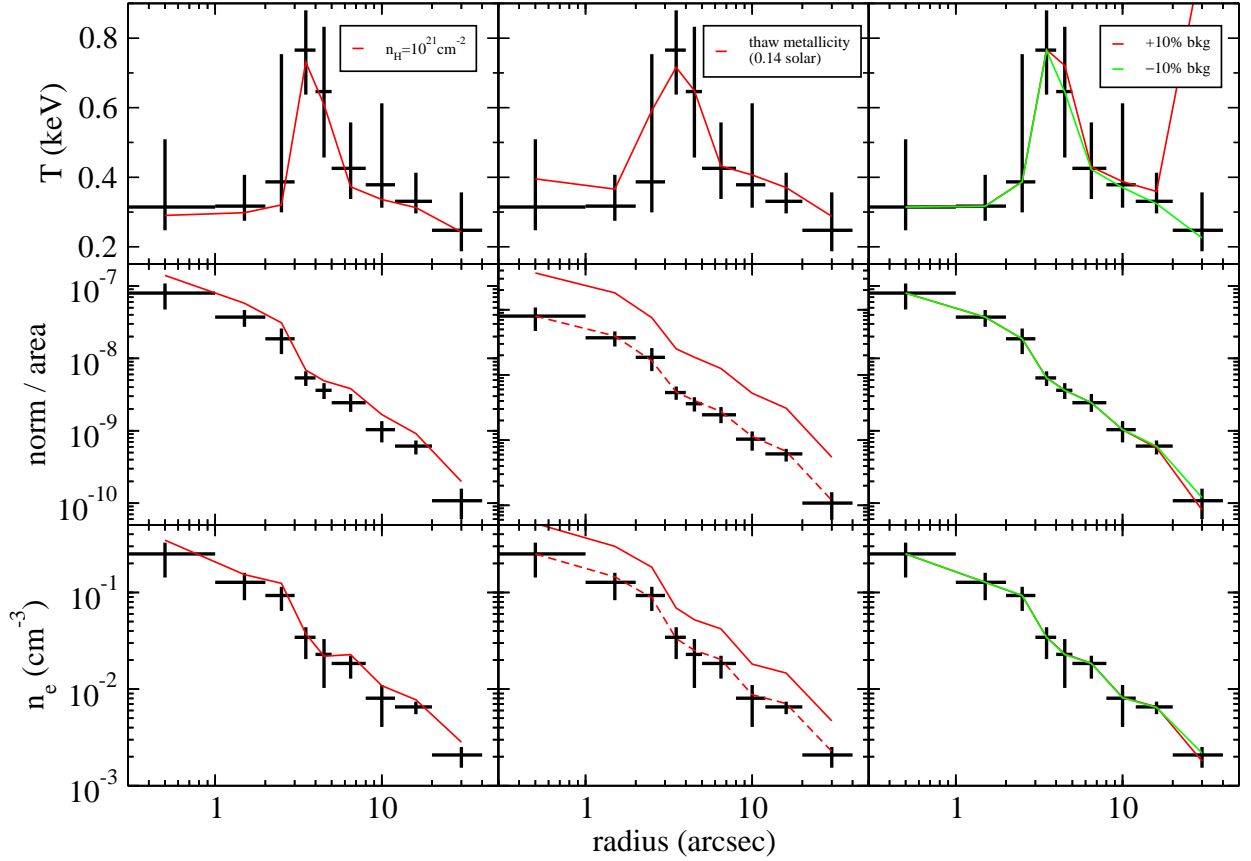


FIG. 10.— Left column: Similar as the left row in Figure 9, but with the red lines representing a model with higher absorption ( $n_{\text{H}} = 10^{21} \text{ cm}^{-2}$ ).

Middle column: Similar as the left row, but with the red lines representing a model with abundance thawed. The best-fit metallicity is 0.14 solar. The red dashed lines in the middle and lower panels represent the same model with abundance thawed but normalized to the nominal model (black) at the central bin. Note that in the middle row panel, the y-axis has a scale slightly different from the other columns. The major tick marks corresponds to those of the other columns.

Right column: Similar as the left row, but with the red (green) lines representing a model with local background level changed by +10 (-10)%.

#### *Metallicity uncertainties*

Fitting the metallicity of the hot gas from X-ray spectra gives a very low abundance of 0.14 solar. However, this sub-solar abundance is not expected since the hot gas should be contributed by stellar feedback which should give solar or super-solar abundance (see, Shcherbakov et al. 2013, for a more detailed discussion). It is also known that metallicity determination can be biased low, particularly due to low spectral resolution of CCDs and multi-temperature structure of the hot gas (Buote 2000; Su & Irwin 2013). Motivated by a more realistic physical situation, we fixed the abundance to the solar value. At temperatures below 1 keV, the emission is dominated by line emission which is proportional to metallicity. This introduces a degeneracy between metallicity and gas density (because emission is also proportional to density squared). Thawing the abundance only introduces a systematic uncertainty in temperature that is smaller than the statistical uncertainty and increases the gas normalizations by a factor of four to five (middle column in Figure 10). The derived density only increases by a factor of two without affecting the density slope. All our conclusions remain the same.

#### *Background uncertainties*

The background only contributes from less than about 1(2)% of the 0.5–2.0 (0.5–6.0 keV) emission at the central 3'' up to 6(10)% at 8''. The background increases to about 50% (60–70%) of the emission in the 0.5–2.0 (0.5–6.0) keV

energy band between 20''–40''. We changed the background level by  $\pm 10\%$ . This generally introduces less than 2% systematic uncertainties in temperature within  $\sim 10''$ , but larger beyond that (right column in Figure 10). The temperature beyond 20'' can be significantly biased. Nevertheless, the gas normalizations is biased by less than 1% within  $\sim 10''$  and at most 25% in the outermost bin (but still smaller than its statistical uncertainty). The bias in the density profile is even smaller. Note that the outermost regions only contribute a small fraction of emission to the projected emission of the inner regions. Therefore, the deprojected density profile of the inner regions is not sensitive to the precise value of the density in the outermost regions.

#### B. X-RAY LIMITS OF THE WEAK AGN

We assessed a conservative upper limit of the potential central point source by modeling the spatial distribution of the X-ray emission in 5'' with a two-component model: a point source component and an extended diffuse component. We model the point source surface brightness profile with a Moffat model. The Moffat model is of the form  $S = S_0[1 + (r/r_c)^2]^{-n}$ , where  $r_c$  and  $n$  are fixed to the best-fit values from a nearby point source, and  $S_0$  is a free parameter which characterizes the contribution of the potential point source. We model the extended diffuse component with another Moffat model and thawed all its three parameters. The best-fit model of the two-component model (Moffat+Moffat) is shown in the right panel of Figure 2. For comparison, we also fitted a single Moffat model (no point source model) and it is plotted on the same figure. We find that a single Moffat model gives  $\chi^2 = 146$  with 97 degrees of freedom for the 0.5–6.0 keV band. The two-component model (Moffat+Moffat) gives  $\chi^2 = 128$  with 96 degrees of freedom. A simple F-test gives an F-statistics of 13.5 with a probability of  $4 \times 10^{-4}$ , strongly suggesting that the two-component model is preferred (or a point source is present). This two-component model suggests that 19-31% (90% confidence interval) of the diffuse emission within a radius of 1'' region in 0.5–6.0 keV comes from the point source. Note that the Moffat model has a flat core, and therefore modeling the extended emission with this model may underestimate the extended emission at the center if the true extended profile is more sharply peaked. Therefore, our estimation of the point source contribution should be regarded as an upper limit.

By performing similar analysis in the soft (0.5–1.0 keV), medium (1.0–2.0 keV), and hard (2.0–6.0 keV) energy bands, we have constrained the photon counts in each of these energy bands from the potential point source. We fit a PHABS\*POWERLAW model using XSPEC to these three energy bands with the absorption fixed at the Galactic value as before. We determined that the best-fit two-component model gives a power-law index of 2.2 with an aperture corrected absorbed luminosity of  $2.9 (0.9) \times 10^{37}$  erg s $^{-1}$  in 0.5–6.0 (0.5–1.0) keV. Using the upper limits of the two-component model gives a power-law index of 2.0 with an aperture corrected absorbed luminosity of  $4.4 (1.1) \times 10^{37}$  erg s $^{-1}$  in 0.5–6.0 (0.5–1.0) keV.

When we included these spectral models for the potential point source in the spectral fitting within a circular region of 1'' in radius, this only increases the best-fit temperature of hot gas (Section 4.1.1) by at most 23% compare to a model without an AGN. Such an increase is much smaller than the statistical uncertainty (90% confidence interval or 95% one-sided uncertainty). The best-fit gas normalization (flux) is at most lowered by about 40%, which is at the lower limit of the 90% confidence interval. Since our model is conservative, we conclude that the potential AGN should not contribute much to the X-ray emission.

#### REFERENCES

- Abramowicz, M. A., Igumenshchev, I. V., Quataert, E., & Narayan, R. 2002, *ApJ*, 565, 1101  
 Baganoff, F. K., et al. 2003, *ApJ*, 591, 891  
 Barai, P., Proga, D., & Nagamine, K. 2012, *MNRAS*, 424, 728  
 Begelman, M. C. 2012, *MNRAS*, 420, 2912  
 Blandford, R. D., & Begelman, M. C. 1999, *MNRAS*, 303, L1  
 Bogdán, Á., & Gilfanov, M. 2011, *MNRAS*, 418, 1901  
 Bondi, H. 1952, *MNRAS*, 112, 195  
 Boroson, B., Kim, D.-W., & Fabbiano, G. 2011, *ApJ*, 729, 12  
 Brighenti, F., & Mathews, W. G. 1999, *ApJ*, 527, L89  
 Brighenti, F., Mathews, W. G., Humphrey, P. J., & Buote, D. A. 2009, *ApJ*, 705, 1672  
 Buote, D. A. 2000, *MNRAS*, 311, 176  
 Buote, D. A., Lewis, A. D., Brighenti, F., & Mathews, W. G. 2003, *ApJ*, 594, 741  
 Das, U., & Sharma, P. 2013, *MNRAS*, 435, 2431  
 Davies, M. B., & King, A. 2005, *ApJ*, 624, L25  
 Dickey, J. M., & Lockman, F. J. 1990, *ARA&A*, 28, 215  
 Di Stefano, R., Greiner, J., Murray, S., & Garcia, M. 2001, *ApJ*, 551, L37  
 Dressler, A., & Gunn, J. E. 1983, *ApJ*, 270, 7  
 Emsellem, E., Dejonghe, H., & Bacon, R. 1999, *MNRAS*, 303, 495  
 Fabian, A. C. 2012, *ARA&A*, 50, 455  
 Fabian, A. C., & Rees, M. J. 1995, *MNRAS*, 277, L55  
 Gayley, K. G. 2013, in American Astronomical Society HEAD Meeting, Two-temperature and Model-Independent Differential Emission Measure Distributions: The Emperor's New Clothes?, ed. American Astronomical Society, 13, 117.02  
 Garcia, M. R., Hextall, R., Baganoff, F. K., Galache, J., Melia, F., Murray, S. S., Primini, F. A., Sjouwerman, L. O., & Williams, B. 2010, *ApJ*, 710, 755  
 Gaspari, M., Ruszkowski, M., & Oh, S. P. 2013, *MNRAS*, 432, 3401  
 Guo, F., & Mathews, W. G. 2013, arXiv:1305.2958  
 Hillel, S., & Soker, N. 2013, *MNRAS*, 430, 1970  
 Ho, L. C. 2008, *ARA&A*, 46, 475  
 Ho, L. C. 2009, *ApJ*, 699, 626  
 Huchra, J., & Burg, R. 1992, *ApJ*, 393, 90  
 Humphrey, P. J., Buote, D. A., Brighenti, F., Gebhardt, K., & Mathews, W. G. 2008, *ApJ*, 683, 161  
 Ichimaru, S. 1977, *ApJ*, 214, 840  
 Irwin, J. A., Athey, A. E., & Bregman, J. N. 2003, *ApJ*, 587, 356  
 Kaastra, J. S., Paerels, F. B. S., Durret, F., Schindler, S., & Richter, P. 2008, *SSRv*, 134, 155  
 Karachentsev, I. D., Karachentseva, V. E., Huchtmeier, W. K., & Makarov, D. I. 2004, *AJ*, 127, 2031  
 Kormendy, J., & Richstone, D. 1992, *ApJ*, 393, 559  
 Kormendy, J., et al. 1996, *ApJ*, 473, L91  
 Kriss, G. A., Cioffi, D. F., & Canizares, C. R. 1983, *ApJ*, 272, 439  
 Ledo, H. R., Sarzi, M., Dotti, M., Khochfar, S., & Morelli, L. 2010, *MNRAS*, 407, 969  
 Li, J., Ostriker, J., & Sunyaev, R. 2013, *ApJ*, 767, 105  
 MacLeod, M., Guillochon, J., & Ramirez-Ruiz, E. 2012, *ApJ*, 757, 134  
 Magorrian, J., & Tremaine, S. 1999, *MNRAS*, 309, 447  
 Mathews, W. G. 1989, *AJ*, 97, 42

- McKee, C. F., & Ostriker, J. P. 1977, *ApJ*, 148
- McNamara, B. R., & Nulsen, P. E. J. 2012, *New Journal of Physics*, 14, 5
- Miller, B., Gallo, E., Treu, T., & Woo, J.-H. 2012, *ApJ*, 747, 57
- Muno, M. P., et al. 2004, *ApJ*, 613, 326
- Narayan, R., & Fabian, A. C. 2011, *MNRAS*, 415, 3721
- Narayan, R., Mahadevan, R., Grindlay, J. E., Popham, R. G., & Gammie, C. 1998, *ApJ*, 492, 554
- Narayan, R., & McClintock, J. E. 2008, *New Astronomy Reviews*, 51, 733
- Narayan, R., & Yi, I. 1994, *ApJ*, 428, L13
- Narayan, R., Igumenshchev, I. V., & Abramowicz, M. A. 2000, *ApJ*, 539, 798
- Pellegrini, S., Baldi, A., Fabbiano, G., & Kim, D.-W. 2003, *ApJ*, 597, 175
- Pellegrini, S., Wang, J., Fabbiano, G., Kim, D.-W., Brassington, N. J., Gallagher, J. S., Trinchieri, G., & Zezas, A. 2012, *ApJ*, 758, 94
- Proga, D., & Begelman, M. C. 2003, *ApJ*, 592, 767
- Quataert, E. 2002, *ApJ*, 575, 855
- Quataert, E., & Gruzinov, A. 2000, *ApJ*, 539, 809
- Quataert, E., & Narayan, R. 2000, *ApJ*, 528, 236
- Randall, S. W., Sarazin, C. L., & Irwin, J. A. 2006, *ApJ*, 636, 200
- Rees, M. J., Begelman, M. C., Blandford, R. D., & Phinney, E. S. 1982, *Nature*, 295, 17
- Revnivtsev, M., Churazov, E., Sazonov, S., Forman, W., & Jones, C. 2007, *A&A*, 473, 783
- Revnivtsev, M., Churazov, E., Sazonov, S., Forman, W., & Jones, C. 2008, *A&A*, 490, 37
- Roberts, M. S., Hogg, D. E., Bregman, J. N., Forman, W. R., & Jones, C. 1991, *ApJS*, 75, 751
- Sage, L. J., & Welch, G. A. 2006, *ApJ*, 644, 850
- Sazonov, S., Sunyaev, R., & Revnivtsev, M. 2012, *MNRAS*, 420, 388
- Sharma, P., McCourt, M., Quataert, E., & Parrish, I. J. 2011, *MNRAS*, 420, 3174
- Shcherbakov, R. V., & Baganoff, F. K. 2010, *ApJ*, 716, 504
- Shcherbakov, R. V., Wong, K.-W., Irwin, J. A., & Reynolds, C. S. 2013, *ApJ*, submitted
- Soker, N., Akashi, M., Gilkis, A., Hillel, S., Papish, O., Refaelovich, M., & Tsebrenko, D. 2013, *Astronomische Nachrichten*, 334, 402
- Su, Y., & Irwin, J. 2013, *ApJ*, 766, 61
- Syer, D., & Ulmer, A. 1999, *MNRAS*, 306, 35
- Tonry, J. L., Dressler, A., Blakeslee, J. P., Ajhar, E. A., Fletcher, A. B., Luppino, G. A., Metzger, M. R., & Moore, C. B. 2001, *ApJ*, 546, 681
- Tremblay, G. R. et al. 2012, *MNRAS*, 424, 1026
- Wilms, J., Allen, A., & McCray, R. 2000, *ApJ*, 542, 914
- Wang, J., & Merritt, D. 2004, *ApJ*, 600, 149
- Wang, J.-M., Cheng, C., & Li, Y.-R. 2012, *ApJ*, 748, 147
- Wang, Q. D., et al. 2013, *Science*, 341, 981
- Wong, K.-W., Irwin, J. A., Yukita, M., Million, E. T., Mathews, W. G., & Bregman, J. N. 2011, *ApJ*, 736, L23 (W11)
- Wong, K.-W., Sarazin, C. L., Blanton, E. L., & Reiprich, T. H. 2008 *ApJ*, 682, 155
- Wrobel, J. M., & Nyland, K. 2012, *AJ*, 144, 160
- Yuan, F., Markoff, S., & Falcke, H. 2002, *A&A*, 383, 854
- Yuan, F., Quataert, E., & Narayan, R. 2003, *ApJ*, 598, 301
- Yuan, F., Wu, M., & Bu, D. 2012, *ApJ*, 761, 129